A constitutive model with microstructure evolution for flow of rate-independent granular materials

J. Fluid Mech. (2011), *vol.* 682, *pp.* 590–616.
doi:10.1017/jfm.2011.251

A constitutive model with microstructure evolution for flow of rate-independent granular materials

JIN SUN[1]† AND SANKARAN SUNDARESAN[2]

[1]School of Engineering, University of Edinburgh, Edinburgh EH9 3JL, UK

[2]Department of Chemical and Biological Engineering, Princeton University, Princeton, NJ 08544, USA

(Received 19 May 2010; revised 27 December 2010; accepted 1 June 2011;
first published online 15 July 2011)

A constitutive model is developed for the complex rheology of rate-independent granular materials. The closures for the pressure and the macroscopic friction coefficient are linked to microstructure through evolution equations for coordination number and fabric. The material constants in the model are functions of particle-level properties and are calibrated using data generated through simulations of steady and unsteady simple shear using the discrete element method (DEM). This model is verified against DEM simulations at complex loading conditions.

Key words: granular media, rheology

1. Introduction

Dense granular materials are ubiquitous in nature and are widely encountered in industrial processes, such as hopper discharge, chute flow, moving beds and standpipe flow. Constituent grains (referred to as particles hereafter) in these materials touch multiple neighbours for finite durations and the stress is largely transmitted through force chains. We focus our attention on one important aspect of dense flow behaviour, namely the rate-independent response, where the inertial effects associated with the individual particle interactions are negligible and the stress is largely independent of the deformation rate.

Many constitutive models have been developed in the literature for rate-independent granular materials. Starting from the basic notion of an 'ideal Coulomb material', where the granular materials are treated as rigid under increasing load until the load reaches a yield point, the models have progressed in terms of incorporating more and more underlying physics. Under a broad category of so-called plastic-potential models (Hill 1950; Harris 2006), work hardening (Drucker, Gibson & Henkel 1957), non-associated flow rules (Lade 1977) and critical state concept (Schofield & Wroth 1968) have been introduced for either rigid-plastic or elastic-plastic materials. Under another category of the double-shearing model, models have been extended from incompressible flows (Spencer 1964) to including dilatancy (Mehrabadi & Cowin 1978), work-hardening (Anand & Gu 2000) and fabric anisotropy (Nemat-Nasser 2000; Zhu, Mehrabadi & Massoudi 2006), which was motivated by the relations

† Email address for correspondence: j.sun@ed.ac.uk

between stress and fabric as observed in experiments using photoelastic particles (Oda, Konishi & Nemat-Nasser 1980; Subhash *et al.* 1991).

More recent experiments (Utter & Behringer 2004; Majmudar & Behringer 2005) and discrete element method (DEM) simulations (Luding 2004, 2005; Aarons, Sun & Sundaresan 2009) further revealed that stress evolution is correlated to microstructure rearrangement during unsteady flow. The jamming transition in dense granular systems profoundly modifies the dynamics and rheology close to the transition (Hébraud & Lequeux 1998; Keys *et al.* 2007; Majmudar *et al.* 2007) and may be related to the onset of rate-independent response. The jamming transition has also been shown to depend on the particle friction coefficient (Song, Wang & Makse 2008).

In this paper, we probe the relation between the rate-independent rheology and the microstructure of a granular material under homogeneous simple shear using DEM simulations, and construct a constitutive model. The main text describes a simple model that neglects normal stress differences, and the extension to include normal stress differences is presented in Appendix A. In this model, the pressure and macroscopic friction coefficient are expressed in terms of microstructural internal variables. Evolution equations are proposed for these internal variables. We correlate the material constants in the model to particle-level properties, such as particle elasticity and friction coefficient. We note at the outset that the present study focuses exclusively on simple shear flows and that the application of this model to completely constrained deformations, such as uniaxial or triaxial compression, will be deferred to future publications.

After describing the DEM and simulation details in § 2, we present simulation results for the evolution of the stress and the internal variables during unsteady shear in § 3. We then detail the development and verification of the constitutive model in §§ 4 and 5, respectively. We summarize the attributes of this model in § 6.

As for notation, we employ lightface italics for scalars, the boldface italic font for vectors and the sans serif bold italic font for the second-order tensors.

2. Computational methods and simulation details

The DEM simulations were carried out using the large-scale atomic/molecular massive parallel simulator (LAMMPS) developed at Sandia National Laboratories (Plimpton 1995). In the simulations, particles interact only at contact. Two spherical particles with position vectors $\{\boldsymbol{r}_i, \boldsymbol{r}_j\}$ and radii $\{R_i, R_j\}$ experience a force, $\boldsymbol{F}_{ij} = \boldsymbol{F}_{n_{ij}} + \boldsymbol{F}_{t_{ij}}$, when $\delta_{ij} = d - r_{ij} > 0$, where $d = R_i + R_j$ and $r_{ij} = |\boldsymbol{r}_{ij}| = |\boldsymbol{r}_i - \boldsymbol{r}_j|$, $\boldsymbol{n}_{ij}$ is the contact normal unit vector pointing from the centre of particle j to that of particle i, and $\boldsymbol{t}_{ij}$ is a unit vector in the tangential plane. The force is calculated using a spring–dashpot model, which has been tested and used in many other studies (Cundall & Strack 1979; Silbert *et al.* 2001, 2007; Campbell 2002; Rycroft, Kamrin & Bazant 2009). The normal and tangential components of the interaction force acting on particle i for the Hookean contact model are

$$\left.\begin{aligned} \boldsymbol{F}_{n_{ij}} &= k_n \delta_{ij} \boldsymbol{n}_{ij} - \gamma_n m^* \boldsymbol{v}_{n_{ij}}, \\ \boldsymbol{F}_{t_{ij}} &= -k_t \boldsymbol{u}_{t_{ij}} - \gamma_t m^* \boldsymbol{v}_{t_{ij}}, \end{aligned}\right\} \tag{2.1a,b}$$

where $k_{n,t}$ and $\gamma_{n,t}$ are the spring elastic and viscous damping constants, $\boldsymbol{v}_{n_{ij}}$ and $\boldsymbol{v}_{t_{ij}}$ are the normal and tangential component of particle relative velocity, respectively, and $m^* = m_i m_j/(m_i + m_j)$ is the effective mass of spheres with masses m_i and m_j. The corresponding contact force on particle j is simply given by Newton's third law, i.e.

$\boldsymbol{F}_{ji} = -\boldsymbol{F}_{ij}$. The tangential force at each contact is computed by keeping track of the elastic shear displacement, $\boldsymbol{u}_{t_{ij}}$, throughout the lifetime of a contact. The elastic shear displacement is set to zero at the initiation of a contact and its rate is given by

$$\frac{\mathrm{d}\boldsymbol{u}_{t_{ij}}}{\mathrm{d}t} = \boldsymbol{v}_{t_{ij}} - \frac{(\boldsymbol{u}_{t_{ij}} \cdot \boldsymbol{v}_{ij})\boldsymbol{r}_{ij}}{r_{ij}^2}. \tag{2.2}$$

The last term in (2.2) arises from the rigid-body rotation around the contact point and ensures that $\boldsymbol{u}_{t_{ij}}$ always lies in the local tangent plane of contact. As the shear displacement increases, the tangential force reaches the limit imposed by a static yield criterion, $|\boldsymbol{F}_{t_{ij}}| \leqslant \mu |\boldsymbol{F}_{n_{ij}}|$, characterized by a local particle friction coefficient, μ. The tangential force is then set to the limit value by truncating the magnitude of $\boldsymbol{u}_{t_{ij}}$.

The contact force according to the Hertzian model is

$$\left.\begin{aligned} \boldsymbol{F}_{nHz_{ij}} &= \sqrt{\delta_{ij} R^*}(k_{nHz}\delta_{ij}\boldsymbol{n}_{ij} - \gamma_n m^* \boldsymbol{v}_{n_{ij}}), \\ \boldsymbol{F}_{tHz_{ij}} &= \sqrt{\delta_{ij} R^*}(-k_{tHz}\boldsymbol{u}_{t_{ij}} - \gamma_t m^* \boldsymbol{v}_{t_{ij}}), \end{aligned}\right\} \tag{2.3a,b}$$

where $R^* = R_i R_j/(R_i + R_j)$ is the effective radius. The normal and tangential elastic constants in the Hertzian model are related to the particle material properties as

$$k_{nHz} = \tfrac{4}{3}E^*, \quad k_{tHz} = 8G^*, \tag{2.4a,b}$$

where $E^* = ([(1-\nu_i^2)/E_i] + [(1-\nu_j^2)/E_j])^{-1}$ and $G^* = ([(2-\nu_i)/G_i] + [(2-\nu_j)/G_j])^{-1}$ with $E_{i,j}$, $\nu_{i,j}$ and $G_{i,j}$ denoting particle Young's modulus, Poisson ratio and shear modulus, respectively. The value of the linear spring elastic constant is chosen to be large enough to minimize particle overlap, yet not so large as to require an unreasonably small simulation time step. In the Hookean model simulations, we set $k_t = 2/7k_n$ (Shäfer, Dippel & Wolf 1996) and $\gamma_t = \frac{1}{2}\gamma_n$, where γ_n is chosen to yield a value of 0.7 for the normal restitution coefficient $e = \exp(-\gamma_n \pi/\sqrt{4k_n/(m^* - \gamma_n^2)})$. In the Hertzian model simulations, the restitution coefficient depends on the initial approaching velocity. Hookean model is used for all results presented except where Hertzian model is explicitly indicated.

In order to maintain homogeneous deformation over large strain scales, we performed the simulations in three-dimensional (3D) periodic domains without gravity. Simple shear flow was induced via the Lees–Edwards boundary conditions (Lees & Edwards 1972). Throughout this study, the x-, y- and z-directions will refer to the flow, neutral (vorticity) and gradient directions, respectively. The shearing motion induced by this boundary-driven algorithm takes time to develop so that the flow would not be homogeneous immediately after a shear rate change, which raises questions about the suitability of the algorithm to study homogeneous time-dependent flows. This disadvantage can be greatly alleviated through the use of the SLLOD algorithm (Evans & Morriss 1990). The SLLOD algorithm implies that a change in the shear rate is not achieved by simply moving the boundaries of the system faster or slower, but by applying a force to the entire system. Thus, the SLLOD algorithm was applied to all the simulations presented in this paper. However, we note that the SLLOD algorithm only affected dynamical behaviour at very small strain scales (typically less than 10^{-3}) after the deformation rate change and did not alter the large strain scale dynamical behaviour in unsteady shear shown in the next section. Thus, we would have obtained essentially the same model even if the SLLOD algorithm was not employed.

Isochoric and dilatant simple shears have been simulated to probe the rheology of the assembly. The isochoric flow was studied under a constant volume (CV) condition

particular to the simulation scheme described above. Experiments of shearing dense granular materials under CV are less common due to dilatancy – a densely packed assembly will expand in volume under initial shear. A pertinent experiment would be the undrained shear test on water-saturated sand, where the volume of the whole specimen can be kept constant within experimental error range (Schofield & Wroth 1968). Since a good rheological model must capture the flow characteristics under all kinds of tests, irrespective of whether such tests are easily implemented in the laboratory or not, we avail the CV simple shear simulations in this study. Dilatant simple shear was examined under constant pressure (CP) condition, where each normal stress component was controlled individually to match that observed in a steady CV simulation. This procedure produces rheological response that can easily be compared to the CV simulations and is essentially the same as that in shear experiments with either free surfaces (Mueth *et al.* 2000; Bocquet *et al.* 2001; Tardos, McNamara & Talu 2003; Toiya, Stambaugh & Losert 2004) or controlled normal loads (Nedderman 1992; Lu, Brodsky & Kavehpour 2007; Kheiripour Langroudi *et al.* 2010) in Couette cells or Jenike shear cells.

Steady state is reached after an assembly is sheared over a large strain (of order unity at least) and the stress and microstructural quantities cease to evolve. The macroscopic rate of deformation tensor at the steady state then follows $\boldsymbol{D} = \frac{1}{2}\dot{\gamma}(\boldsymbol{e}_{(x)}\boldsymbol{e}_{(z)} + \boldsymbol{e}_{(z)}\boldsymbol{e}_{(x)})$, where $\boldsymbol{e}_{(x)}$ and $\boldsymbol{e}_{(z)}$ are unit vectors in the x- and z-directions, respectively, and $\dot{\gamma}$ is the flow velocity gradient (the shear rate). The type of unsteady flows studied here is shear reversal flow, where the flow direction is reversed after the steady state is reached and maintained for a certain strain. In this case, $\dot{\gamma}$ changes its sign after reversal. The shear rate is maintained low in the sense that the inertia number (MiDi 2004) (or Weissenberg number, Goddard 1986), $I = \dot{\gamma} d/(\sqrt{p/\rho_s \phi})$, where p is a confining pressure, ρ_s is particle density and ϕ is particle volume fraction, is smaller than 10^{-3}, so that the rate-independent response is guaranteed according to previous experimental and simulation data (Campbell 2002; MiDi 2004; da Cruz *et al.* 2005; Aarons *et al.* 2009).

Homogeneous stress and strain can be extracted from this type of flows, which facilitates constitutive modelling. The macroscopic stress is calculated as

$$\boldsymbol{\sigma} = \frac{1}{V}\sum_i \left[\sum_{j\neq i} \frac{1}{2}\boldsymbol{r}_{ij}\boldsymbol{F}_{ij} + m_i(\boldsymbol{v}_i')(\boldsymbol{v}_i')\right], \tag{2.5}$$

where V is the total volume of the simulation domain and $\boldsymbol{v}_i'$ is the fluctuating velocity of a particle relative to its mean streaming velocity in the shear flow. The first and the second terms on the right-hand side of (2.5) represent the contact force contribution and the inertial effect associated with particle streaming, respectively. In all the results presented, the second term was at least four orders of magnitude smaller than the first term, consistent with the rate-independent response.

3. Unsteady shear rheology

In this paper, we present and analyse the results obtained in simulations of an assembly of 2000 monodisperse spheres in a 3D periodic domain. The dependence on system size, i.e. particle number, was tested using assemblies with particle numbers varying from 1000 to 10 000 and it was found that a system size of 2000 particles was sufficient to get stress and microstructural data that are independent of size. All the results presented here are ensemble averages of 10–20 realizations with different initial configurations.

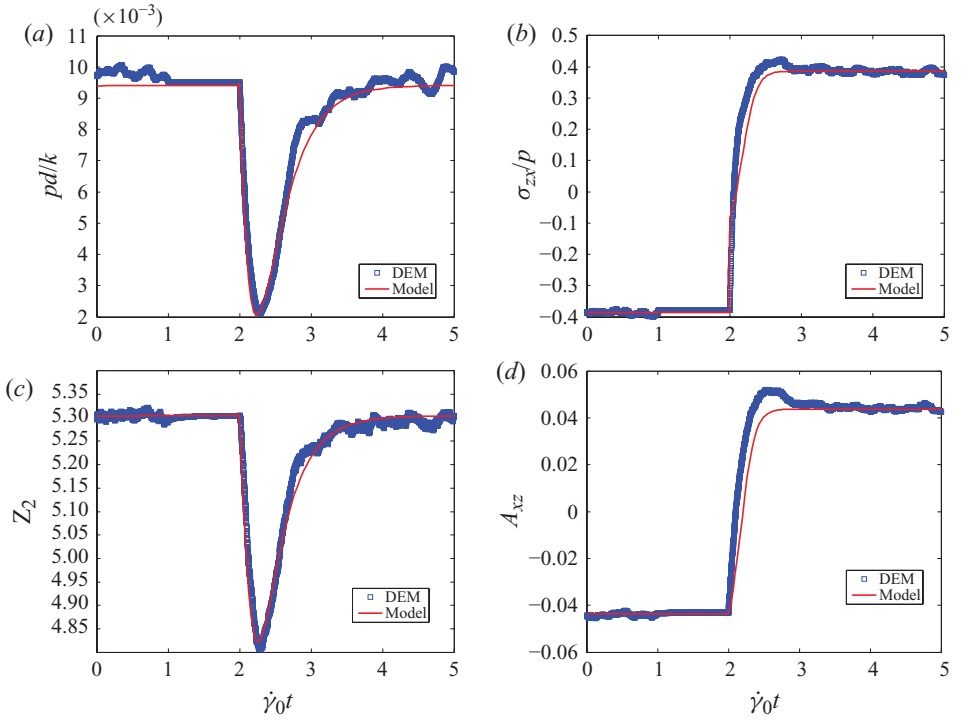

FIGURE 1. (Colour online available at journals.cambridge.org/flm) Evolution of (a) scaled pressure pd/k (where $k = k_n$), (b) stress ratio, (c) coordination number and (d) A_{xz} for an assembly subjected to unsteady shear under the constant volume condition with $\phi = 0.60$. Blue square symbols denote the data from DEM simulations and the red solid curves are the constitutive model results. The shearing was stopped during $1 < \dot{\gamma}_0 t < 2$. The interparticle friction coefficient μ is 0.5 and the inertia number $I \approx 0.0003$ at steady state.

An assembly with particle volume fraction ϕ of 0.6 was first sheared at a shear rate of $\dot{\gamma}_0 = 2|\boldsymbol{D}_0|$, where $|\boldsymbol{D}_0|$ is the modulus of the initial strain rate tensor ($:= \sqrt{\frac{1}{2}\boldsymbol{D}_0^{\mathrm{T}} : \boldsymbol{D}_0}$), to reach a statistical steady state under the CV condition and the time $t = 0$ was chosen as an arbitrary state in this statistical steady state. The assembly was then subjected to a specific shear pattern as described below. Figure 1 shows the variation of various statistical quantities with accumulated shear strain $\dot{\gamma}_0 t$. The shearing was stopped at $\dot{\gamma}_0 t = 1$, and hence the quantity $\dot{\gamma}_0 t$ within the range of $1 < \dot{\gamma}_0 t < 2$ should be interpreted as a non-dimensional time measure. The pressure scaled by particle diameter and elastic spring constant, and the shear stress-to-pressure ratio are shown in figures 1(a) and 1(b), respectively. They clearly exhibited a rate-independent response as the stress level was retained during the no-shear period ($1 < \dot{\gamma}_0 t < 2$) with little change from the steady state. The rate-independent characteristic has also been verified by collapsing the stress data from simulations at various values of shear rates; those results add no significant information and are not shown in the figures. At $\dot{\gamma}_0 t = 2$, the flow direction was reversed and the shear rate became $\dot{\gamma} = -\dot{\gamma}_0$. The pressure and stress ratio exhibited significant variations over strain intervals of order unity following the reversal. The pressure dropped to a lower value and slowly returned to the steady state. As the volumetric strain was kept at zero, this behaviour rules out volume fraction change as a necessary cause of the pressure variation. The

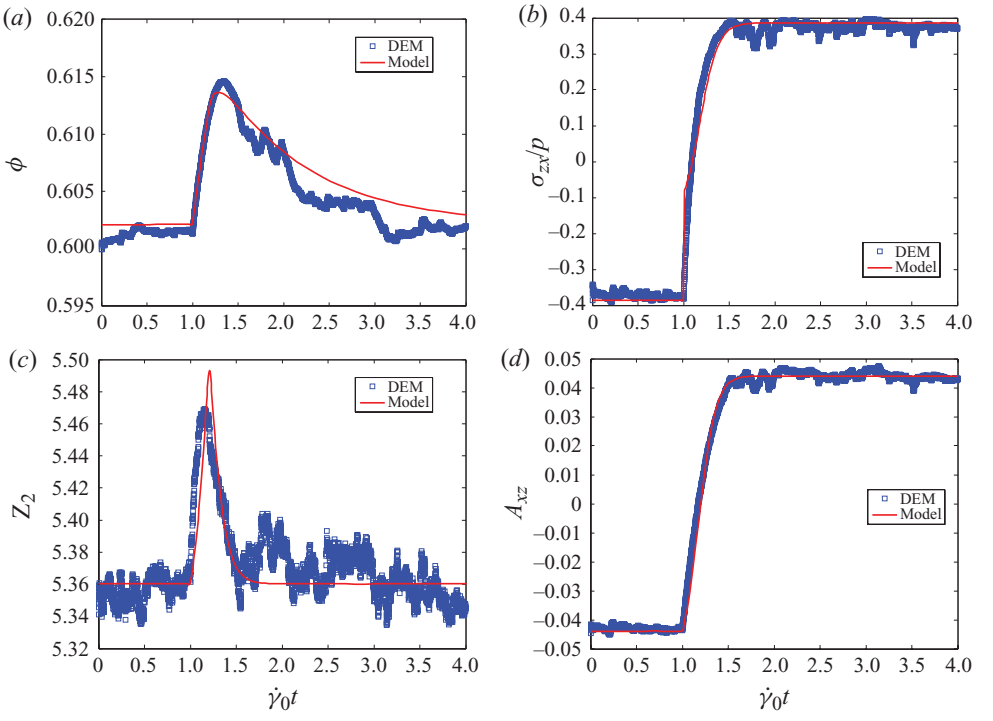

FIGURE 2. (Colour online) Evolution of (*a*) volume fraction, (*b*) stress ratio, (*c*) coordination number and (*d*) A_{xz} for an assembly subjected to unsteady shear under the constant pressure condition. Blue square symbols denote the data from DEM simulations and the red solid curves are the constitutive model results. The interparticle friction coefficient μ is 0.5 and the inertia number $I \approx 0.0003$ at steady state.

steady-state magnitude of the stress ratio is about 0.4, which was close to the measured quasi-static value in a shear cell experiment using polystyrene beads (Savage & Sayed 1984). Upon shear reversal, the stress ratio slowly evolved to a new steady-state value with the same magnitude as the initial state, but with an opposite sign. A similar stress variation trend after shear reversal has also been observed in experiments with dense granular materials (Toiya *et al.* 2004; Utter & Behringer 2004) and with dense suspensions (Gadala-Maria & Acrivos 1980).

For the case in which the assembly was sheared under the CP condition, the volume fraction and stress ratio (see figures 2*a* and 2*b*, respectively) manifested variations after shear reversal at $\dot{\gamma}_0 t = 1$. The volume fraction increased at first (the assembly compacted) and then decreased (the assembly dilated) back to the steady state after a shear strain of about 0.5. The compaction behaviour was also reported in the Couette shear cell experiment after shear reversal (Toiya *et al.* 2004). The stress ratio evolution had a similar trend as that in the constant volume case.

To further investigate the mechanism of this variation due to shear reversal, we studied the microstructure evolution during this unsteady shear. We quantified the microstructure using two variables, the average (mechanical) coordination number Z and the fabric tensor $\boldsymbol{A}$. The average (mechanical) coordination number is defined as the mean contacts per particle in the contact network, $Z = 2N_c/N$, where N_c is the total number of contacts (with non-zero contact forces) and N is the total number of particles in the contact network (Zhang & Makse 2005). It characterizes

the connectivity of a granular assembly. When the coordination number is equal to a critical value Z_c, the granular assembly is at an isostatic state, where the number of degrees of freedom is matched by the number of constraints between particles. Z_c varies from 4 to 6 as particle friction coefficient changes from infinity to zero in three dimensions (Song *et al.* 2008). Z_c is a microstructural signature of the jamming transition (O'Hern *et al.* 2003; Song *et al.* 2008), and can also be identified as a critical point, above which rate-independent behaviour is found. In the computation of Z from our DEM data, we neglect particles with zero (floaters) or one contact (rattlers) as they do not participate in the contact network, consistent with the practice of other researchers (Shundyak, van Hecke & van Saarloos 2007). In any case, floaters and rattlers make up only a very small portion of total particles in our simulations. We henceforth use the symbol Z_2 to distinguish from those including floaters and rattlers and we only used Z_2 to calibrate our model constants.

The fabric tensor was used to characterize microstructure anisotropy. It can be understood as a statistical moment with respect to the probability distribution function of an orientational vector $\boldsymbol{n}$. With different choices of the vector $\boldsymbol{n}$ and weighting factors, there have been various definitions (Oda *et al.* 1980; Bathurst & Rothenburg 1990; Goddard 1998; Radjai *et al.* 1998; Azéma, Radjai & Saussine 2009). In this paper we identify $\boldsymbol{n}$ as the unit contact normal vector pointing from centre to centre of two spherical particles in contact. We define the fabric tensor as the symmetric traceless second rank tensor

$$\boldsymbol{A} = \frac{1}{N_c}\sum_{\alpha=1}^{N_c} \boldsymbol{n}^{\alpha}\boldsymbol{n}^{\alpha} - \frac{1}{3}\boldsymbol{I}, \tag{3.1}$$

where $\boldsymbol{I}$ is the unit tensor. Its eigenvectors give the principal directions of the mean contact orientations. The eigenvalues, in turn, provide a measure of the extent to which contacts are oriented in the principal directions. We may use the difference between the largest (major) and smallest (minor) eigenvalues or the second invariant as a measure of the anisotropy. That being said, the structural anisotropy can be easily related to the shear (xz) component of the fabric tensor for simple shear flows; our DEM data show that the numerical values of A_{xx} and A_{zz} are small in magnitude compared to A_{xz}, while A_{yy}, A_{xy} and A_{yz} are essentially zero. The off-diagonal terms A_{xz} and A_{zx} are larger than the diagonal terms by at least an order of magnitude, and so the difference between the major and minor eigenvalues is very close to $2A_{xz}$ and the corresponding eigenvectors lie in the x–z plane at an angle of $\pm 45^{\circ}$ to the x-axis. Thus, we present below the magnitude of A_{xz} as a measure of anisotropy and the sign of A_{xz} for the orientation of the principal direction in simple shear flows.

The evolution of Z_2 and A_{xz} is plotted in figures 1(c) and 1(d) for the CV case. It can be immediately recognized that Z_2 and A_{xz} have evolution patterns similar to the pressure and stress ratio, respectively. The Z_2 values held up during the no-shear phase ($1 < \dot{\gamma}_0 t < 2$)), decreased significantly after the shear reversal and returned to the steady-state value after the same strain scale as the pressure did. The variation of the coordination number after shear reversal indicates that the contacts were broken at first and subsequently built up. The A_{xz} variation shows that the microstructure lost its anisotropy and then slowly re-established the anisotropy with a principal direction rotated by 90° over a comparable strain scale as the shear stress-to-pressure ratio did. The simultaneous evolution of the two variables revealed the microstructural rearrangement after shear reversal, which involved both connectivity and anisotropy changes and had a strain scale of $\sim$1. During the CP shear, large-scale microstructural

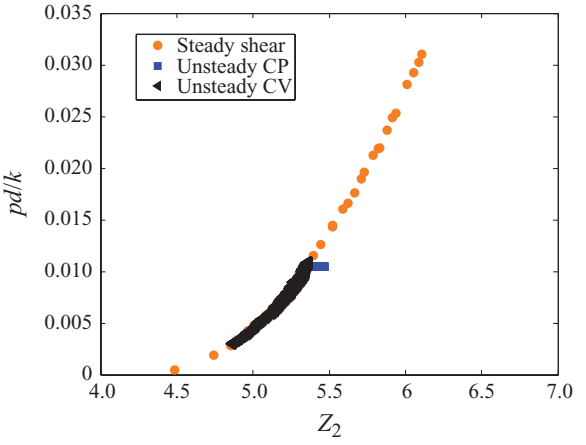

FIGURE 3. (Colour online) Scaled pressure variations against coordination number for simulations of steady and unsteady shear under both constant volume (CV) and constant pressure (CP) conditions. The interparticle friction coefficient μ is 0.5.

rearrangement was also indicated by the evolution of Z_2 and A_{xz} in figures 2(c) and 2(d). The Z_2 increased a small amount after the shear reversal. Since the pressure was maintained constant for the entire shearing process, this increase suggests that pressure is influenced by the anisotropy in addition to the coordination number. The evolution of A_{xz} (see figure 2d) again mirrors that of the stress ratio.

4. Constitutive model formulation and calibration

We will demonstrate that a simple model of the form

$$\boldsymbol{\sigma} = p\boldsymbol{I} - p\eta\hat{\boldsymbol{S}}, \tag{4.1}$$

where $\hat{\boldsymbol{S}} := \boldsymbol{S}/|\boldsymbol{D}|$ and $\boldsymbol{S}$ is the deviatoric strain rate tensor ($\boldsymbol{S} = \boldsymbol{D} - \frac{1}{3}\mathrm{tr}(\boldsymbol{D})\boldsymbol{I}$) and η is a scalar macroscopic friction coefficient, is enough to capture the dynamic shear results, provided p and η are expressed in terms of Z_2 and $\boldsymbol{A}$, and suitable evolution equations are postulated for these microstructural quantities. This stress equation can be considered as a simplified version of a rate-independent rheological model (Goddard 1984, 2006). It can also be derived from a plasticity model assuming a pressure-dependent yield function and a co-axial flow rule (Schaeffer 1987). We demonstrate in Appendix A how the model can be extended to include normal stress differences present in shear flows.

4.1. *The pressure and η relations*

Granular pressure has been modelled as a function of particle volume fraction in elasticity (Makse, Johnson & Schwartz 2000; O'Hern *et al.* 2003), or at the critical state of plastic flow (Schofield & Wroth 1968). However, neither the elastic pressure nor the critical state pressure relations can be generalized to unsteady flow, as is evident from the pressure variation under CV or volume fraction variation under CP in figures 1 and 2, respectively. By using coordination number as a state variable, we are able to collapse the pressure data for steady and unsteady shear quite well with smooth functional dependence as shown in figure 3. The small discrepancy between the unsteady and steady shear data is attributed to the anisotropy variation during shear reversal.

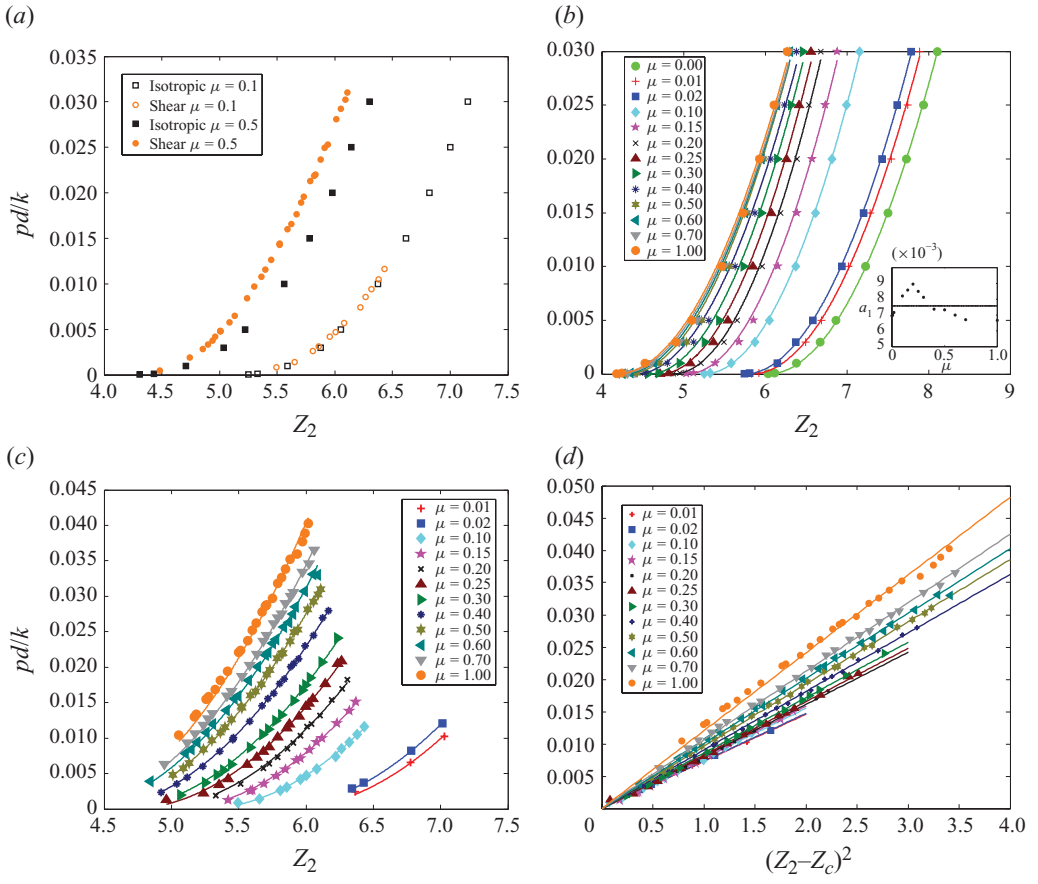

FIGURE 4. (Colour online) (*a*) Scaled pressure variations against the coordination number for isotropic compression and steady simple shear with open and filled symbols used for assemblies with interparticle friction coefficient $\mu = 0.1$ and $\mu = 0.5$, respectively; the same variation for (*b*) isotropic compression and (*c*) steady simple shear for assemblies with interparticle friction coefficient μ ranging from 0 to 1; the data in (*c*) are re-plotted against $(Z_2 - Z_c)^2$ in (*d*). The symbols in the figures denote the DEM data; the solid lines in (*b*) show the fits using $pd/k = a_1(Z_2 - Z_c)^2$; the solid lines in (*c*) and (*d*) indicate results from the model of $pd/k = (0.0073 + a_2|\boldsymbol{A}|)(Z_2 - Z_c)^2$. The inset in (*b*) shows the variation of fitting parameter a_1 versus μ.

According to these features, we model the pressure (attributed to contact force) as a function of Z_2 and $\boldsymbol{A}$:

$$pd/k = (a_1 + a_2|\boldsymbol{A}|)(Z_2 - Z_c)^{\alpha}, \tag{4.2}$$

where a_1 and a_2 are material parameters and $\alpha = 2$. The pressure in an isotropic state, modelled by the $a_1(Z_2 - Z_c)^{\alpha}$ term, was examined using stress-controlled isotropic compression. (Details of the simulation protocol are presented in Appendix B. Under isotropic compression, the pressure manifested a dependence on the packing preparation history, e.g. on the initial volume fractions before compression (Song *et al.* 2008). Details of our approach of modelling this history dependence and the rationale of simplifying the relation are discussed in Appendix B.) The values of pressure in both isotropic compression *at the infinite compactivity limit* and steady simple shear are plotted as functions of Z_2 for $\mu = 0.1$ and $\mu = 0.5$ in figure 4(*a*). It

can be seen that the pressure starts to be measurable when Z_2 is greater than Z_c for both isotropic compression and simple shear. Thus, Z_c is identified as the transition point above which granular systems exhibit dynamics dominated by their jammed structures, and manifest rate independence when subjected to simple shear flows. The pressure in simple shear flow is, however, higher than that in the isotropic state at the same coordination number, which is reflected in (4.2).

We calibrate the a_1 term on the right-hand side in (4.2) using the isotropic compression data and the a_2 term using the simple shear data. The variation of pressure under isotropic compression with the coordination number is shown in figure 4(*b*) for assemblies with μ ranging from 0 to 1. We determined the Z_c values by first extrapolating these DEM data to the zero pressure limits and then fine-tuning them as a fitting parameter in the equation of $pd/k = a_1(Z_2 - Z_c)^2$, which has the same form as the critical scaling shown for frictionless particles near jamming transition (O'Hern *et al.* 2003). The goodness of the fit in figure 4(*b*) indicates that this scaling is essentially universal for frictional particles with fitting parameter a_1 fluctuating in a small range as shown in the inset of figure 4(*b*). The weak dependence of a_1 on μ was also observed in 2D simulations of ploydisperse particles (Somfai *et al.* 2007). In favour of simplicity of the model, a_1 is approximated as a constant independent of μ. Particle friction plays the role of shifting Z_c, but does not affect the scaling in any significant way. The critical coordination number Z_c monotonically decreases from 6 towards 4 for increasing finite μ values as indicated by our DEM data (see figure 5*a*). We note that Z_c should have numerical values of 6 and 4 at $\mu = 0$ and $\mu = +\infty$, respectively; these values are determined by the isostatic state at jamming transition (Song *et al.* 2008). However, a fit with a plateau value slightly higher than 4 is used to better represent our DEM data for μ in the range of 0–1.

The material parameter a_2 was calibrated using the data from steady simple shear DEM simulations, shown by symbols in figure 4(*c*). Fits of pressure against Z_2 and $(Z_2 - Z_c)^2$ using (4.2) with a fixed a_1 are illustrated by solid lines in figures 4(*c*) and 4(*d*), respectively. The fitting parameter a_2 increases monotonically with μ as indicated by the increasing slopes in figure 4(*d*). Simple shear data for $\mu = 0$ had a low confidence level due to the large fluctuations of coordination numbers observed in the simulations of high volume fractions and are not shown in this figure. However, the variation of a_2 versus μ is clearly monotonic and can be fitted using a linear function $a_2 = x_1\mu$ as shown in figure 5(*b*). The vanishing of a_2 at the $\mu = 0$ limit is also consistent with the physics that the anisotropy contribution to pressure vanishes at the frictionless limit, which can be inferred from the absence of dilatancy for frictionless spheres observed in our simulations and also in the 3D simulations of Peyneau & Roux (2008). The inference will become clear after we introduce the microstructure evolution equation. The numerical values of a_1 and the parameter x_1 for a_2 are listed in table 1.

The scaling in (4.2) did depend on force models used in simulations. Accordingly, for a physical particle assembly, this means that the elasticity of particles affects the pressure scaling of the assembly. This can be seen from a micromechanical equation

$$\boldsymbol{\sigma} \approx= \frac{3\phi Z}{2\pi d^3}\bar{r}\left(k_n\bar{\delta}_n\frac{1}{N_c}\sum_i\sum_{j\neq i}\boldsymbol{nn} - k_t\bar{\delta}_t\frac{1}{N_c}\sum_i\sum_{j\neq i}\boldsymbol{nt}\right), \tag{4.3}$$

where $\bar{r}$, $\bar{\delta}_n$ and $\bar{\delta}_t$ are mean quantities. The pressure for particles with Hertzian contact can then be shown to have a 3/2 power relation with that for particles with

	α	a_1	a_2	a_3	a_4	b_1	b_2	Z_c	ϕ_c
x_1	2	0.0073	−0.1	1.57	−6	−0.16	1.6	1.85	0.058
x_2				−4.5	−2	−6	−6	−5	−5
x_3				−1.7	6	0.16	−2.9	4.15	0.582

TABLE 1. Numerical values of α, a_1 and x_1–x_3 in the fitting expressions, $x_1\mu$ and $x_1 e^{x_2\mu} + x_3$, for the material parameters in the pressure and η equations, and the Z_2 evolution equation.

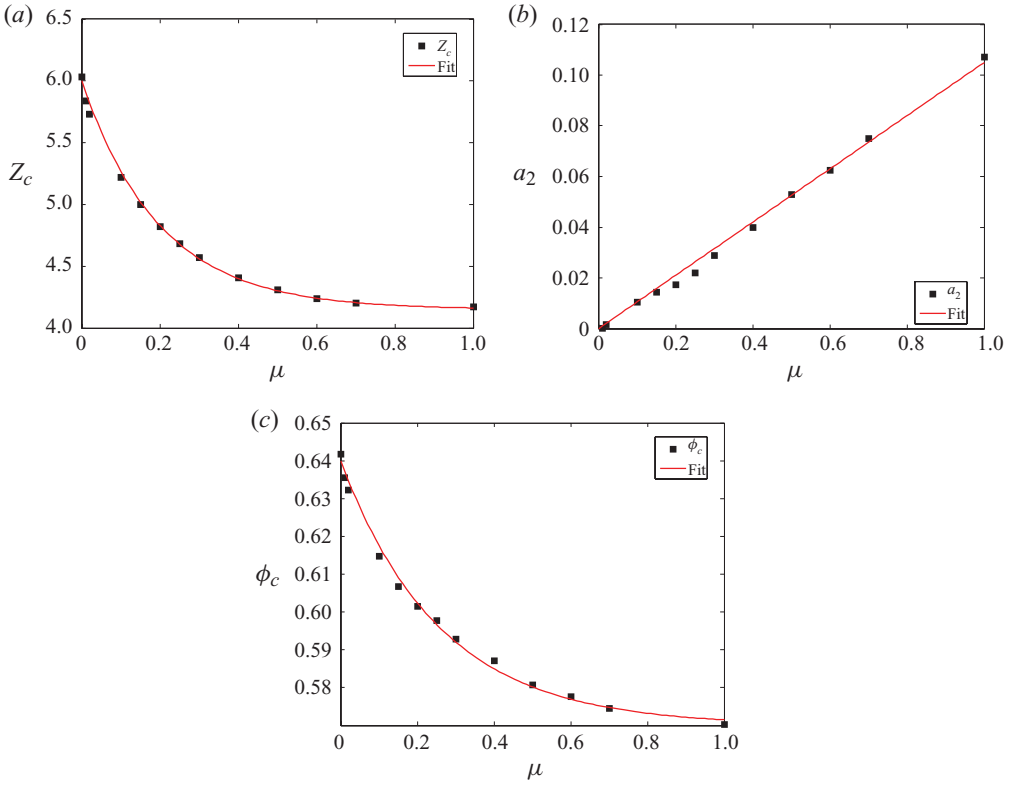

FIGURE 5. (Colour online) Variations of (a) the critical coordination number Z_c, (b) the material parameter, a_2, in the pressure equation and (c) the critical volume fraction ϕ_c with respect to the interparticle friction coefficient, μ.

Hookean contact, i.e.

$$\frac{p_{Hz}}{k_{Hz}} \sim \left(\frac{p_{Hk}d}{k}\right)^{3/2}, \tag{4.4}$$

where k_{Hz} and k are the normal elastic constants for Hertzian and Hookean contact models, respectively. This power relation was confirmed by collapsing our DEM data of pressure from the two models using this relation, as illustrated in figure 6.

The shear stress-to-pressure ratio in figures 1 and 2 was shown to have an evolution pattern similar to the shear component of the fabric tensor A_{xz}. Figure 7 shows a plot of the stress ratio during a shear reversal under constant volume condition (the same data as in figure 1b) against A_{xz}. The data for unsteady shear under constant pressure would collapse essentially onto the same curve and hence, for sake of brevity, is not

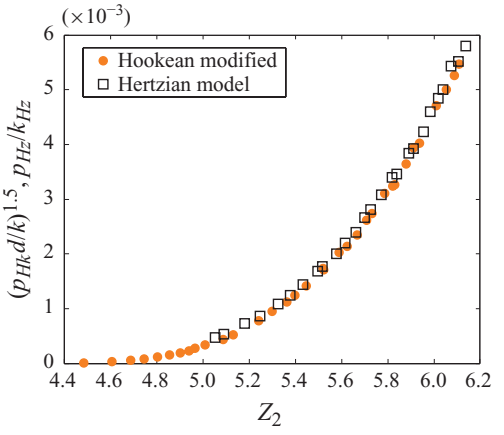

FIGURE 6. (Colour online) Pressure versus coordination number for simulations using the Hookean and Hertzian contact models in steady simple shear. The Hookean model data collapse with the Hertzian model data after using a 3/2 power scaling. The interparticle friction coefficient is 0.5.

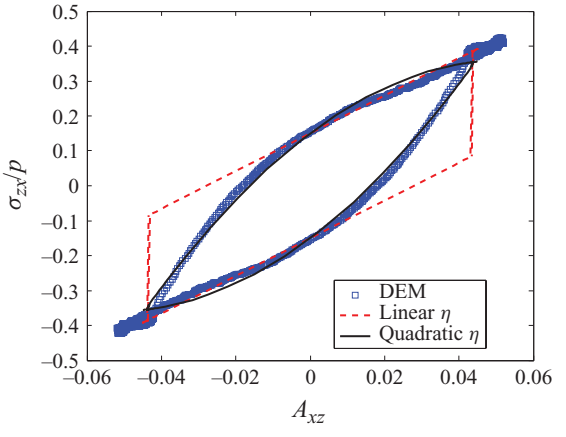

FIGURE 7. (Colour online) Stress ratio variations against the shear component of the fabric tensor for unsteady simple shear. Symbols, dashed lines and solid lines in the figure denote the DEM results, model results using the linear and quadratic η equations, respectively. The assembly is subjected to unsteady shear under the constant volume condition with $\phi = 0.60$ and $\mu = 0.5$ and the inertia number $I \approx 0.0003$ at steady state.

plotted. The two branches show how the stress ratio evolved from one steady state to the other and back. Figure 7 suggested a model for η,

$$\eta = b_1 + b_2 \boldsymbol{A} : \hat{\boldsymbol{S}}, \tag{4.5}$$

where the b values are material constants. The stress ratios calculated from (4.5) are plotted in (red) dashed lines and compared with the DEM data in figure 7. This equation yields only linear approximation of the DEM results but captures most of the stress ratio variation except immediately after shear reversal. A quadratic relation,

$$\eta = \hat{b}_1 + \hat{b}_2 \boldsymbol{A} : \hat{\boldsymbol{S}} + \hat{b}_3 (\boldsymbol{A} : \hat{\boldsymbol{S}})^2, \tag{4.6}$$

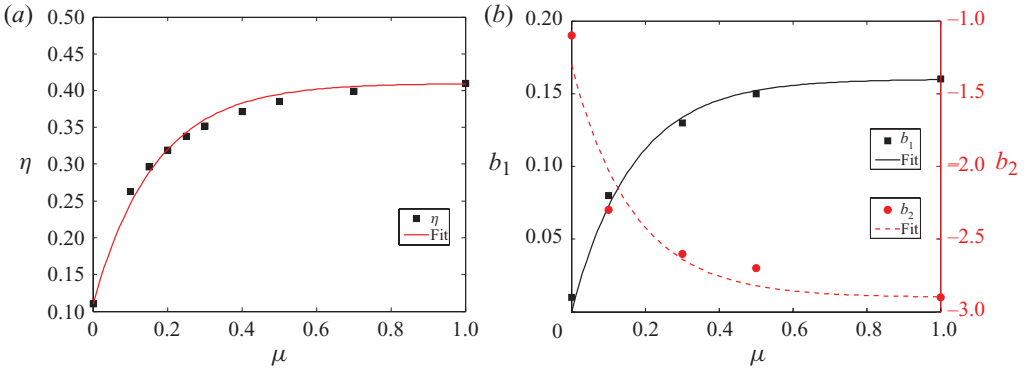

FIGURE 8. (Colour online) (*a*) Variation of η versus μ during steady simple shear. (*b*) Correlations of b_1 and b_2 with μ are shown using the left and right y-axes, respectively. The equations used for the fitting curves in (*a*) and (*b*) are $\eta = -0.3e^{-6\mu} + 0.41$, $b_1 = -0.16e^{-6\mu} + 0.16$ and $b_2 = 1.6e^{-6\mu} - 2.9$, respectively.

shown by (black) solid lines in figure 7 better approximates the stress ratio variation. However, the strain extents where (4.5) and (4.6) differed significantly were very small. We therefore employ (4.5) for the constitutive model in this paper as it has one less fitting parameter.

The η value for steady shear was found to increase with μ and reach a plateau value at large μ values as shown in figure 8(*a*). It does not vanish for frictionless particles ($\mu = 0$), indicating a non-zero macroscopic friction. This is consistent with the findings of Peyneau & Roux (2008); the internal friction angle $\varphi = \arctan(\eta)$ found in our study is about 5.7°, which is close to the value $5.76° \pm 0.02°$ reported by them (Peyneau & Roux 2008). For $\mu = 0.5$ or higher, η is about 0.4 (see figure 8*a*), which is very close to the ratio of shear to normal stress for polystyrene beads in the shear cell experiment reported by Savage & Sayed (1984). The η versus μ relation is consistent with data from other experimental or computational studies (Thornton 2000; Suiker & Fleck 2004; Ketterhagen *et al.* 2009).

The correlations of the model parameters, b_1 and b_2, with the friction coefficient μ were established using the simulation data (see figure 8*b*). A functional form $x_1 e^{x_2\mu} + x_3$ was employed for these correlations, the numerical values for which are listed in table 1. Coefficient b_1 was found to be essentially zero at $\mu = 0$ within numerical errors of the DEM simulations. The vanishing of b_1 can also be understood from the micromechanical stress (4.3): without particle friction, the tangential force contribution to stress (the second term on the right-hand side of the equation) disappears and the deviatoric stress is then proportional to the fabric (in the first term on the right-hand side of the equation), to satisfy which b_1 has to be zero in (4.5). Physically, this means that anisotropy is the sole contribution to macroscopic friction at the frictionless particle limit. In contrast, b_1 is non-zero for frictional particles (see figure 8*b*), which indicates that macroscopic friction exists even when anisotropy is zero because tangential forces contribute to the deviatoric stress for frictional particle assemblies.

4.2. *Microstructure evolution equations*

To complete the constitutive model, appropriate evolution equations for the microstructural variables are required. Stress can then be evolved through microstructural evolution for unsteady flow. On the basis of the DEM results for

c_1	c_2	c_3	d_1	d_2	d_3	β_1	β_2
−0.52	−2.8	100	−45	5.6	−40	7.5	0.5

TABLE 2. Numerical values of the material parameters in the microstructure evolution equations.

microstructure evolution, we model the rate of change of both $\boldsymbol{A}$ and Z_2 as functions of $\boldsymbol{A}$ and $\boldsymbol{D}$. We postulate the following evolution equation for the fabric:

$$\mathring{\boldsymbol{A}} = c_1\boldsymbol{S} + c_2|\boldsymbol{D}|\boldsymbol{A} + c_3(\boldsymbol{A}:\boldsymbol{S})\boldsymbol{A}. \tag{4.7}$$

Here, $\mathring{\boldsymbol{A}} = \dot{\boldsymbol{A}} + \boldsymbol{A}\cdot\boldsymbol{W} - \boldsymbol{W}\cdot\boldsymbol{A}$, where $\boldsymbol{W}$ is the spin tensor, $\boldsymbol{W} = \frac{1}{2}(\nabla\boldsymbol{v} - (\nabla\boldsymbol{v})^{\mathrm{T}})$, and $\dot{\boldsymbol{A}}$ denotes its material time derivative. It can be readily ascertained that this evolution equation preserves rate independence and that the fabric evolves with strain extent.

An inspection of the simple shear flow results revealed a small (about 10 %), but systematic decrease in the modulus of fabric, $|\boldsymbol{A}| = \sqrt{\frac{1}{2}\boldsymbol{A}^{\mathrm{T}} : \boldsymbol{A}}$, with increasing volume fraction for each μ value studied. For the purpose of the present modelling effort, this variation is deemed unimportant and so we approximate the fabric as being essentially independent of volume fraction. The values of $|\boldsymbol{A}|$ obtained at various volume fractions were averaged to obtain a typical value for steady shear flow. We have also assumed that $|\boldsymbol{A}|$ in the model is independent of μ as well, which was confirmed to hold for $\mu > 0.1$. Thus c_1–c_3 in (4.7) are simply constants; their numerical values deduced from the shear reversal data are listed in table 2. (This μ-independent $\boldsymbol{A}$ was used while determining the parameters a_2 and b_2 described earlier for self-consistency.)

It should be noted that this evolution equation was not derived from first principles; instead, it was devised to yield the desired response. The first term on the right-hand side was introduced to recognize that shear induces anisotropy; the second term (with $c_2 < 0$) stabilises the system and allows a steady state to be established at large strain. The third term plays a mixed role – following shear reversal, it is destabilizing initially and plays a stabilizing role at later stages. This dual role permits a degree of control over the response. Throughout this study, we tried to restrict the model to include only $\boldsymbol{A}$, $|\boldsymbol{A}|$, $\hat{\boldsymbol{D}}$, $|\hat{\boldsymbol{D}}|$ and $\boldsymbol{A}\hat{\boldsymbol{D}}$; this was achieved for all the equations except the $\boldsymbol{A}$ evolution equation where we added the third term on the right-hand side to give an extra flexibility in capturing the transition. We solved (4.7) for homogeneous simple shear and compared to the DEM results in figures 1(d) and 2(d). It can be seen that (4.7) is able to capture quite well the steady state and the evolution of A_{xz}. Such comparisons were ascertained at several different values of μ and ϕ.

The need to evolve the coordination number has been recognized in the literature earlier. For example, Gera, Syamlal & O'Brien (2004) proposed a heuristic evolution equation for Z in the context of the two-fluid modelling of fluidized beds; while Rothenburg & Kruyt (2004) postulated an evolution equation for planar granular materials. We postulate the following rate-independent evolution equation for the coordination number Z_2:

$$\dot{Z}_2 = d_1(\boldsymbol{A}:\boldsymbol{S} - \chi|\boldsymbol{S}|) + d_2|\boldsymbol{D}|(f(\phi) - Z_2) + d_3\mathrm{tr}(\boldsymbol{D}), \tag{4.8}$$

where $\chi = -(c_2 + \sqrt{c_2^2 - 8c_1c_3})/2c_3$ equals $\boldsymbol{A} : \hat{\boldsymbol{S}}$ for steady simple shear according to (4.7) and d_1–d_3 are material constants. (As discussed in Appendix B this equation is limited to deformations with $|\mathrm{tr}(\hat{\boldsymbol{D}})| \ll 1$.) The first two terms and the fourth term

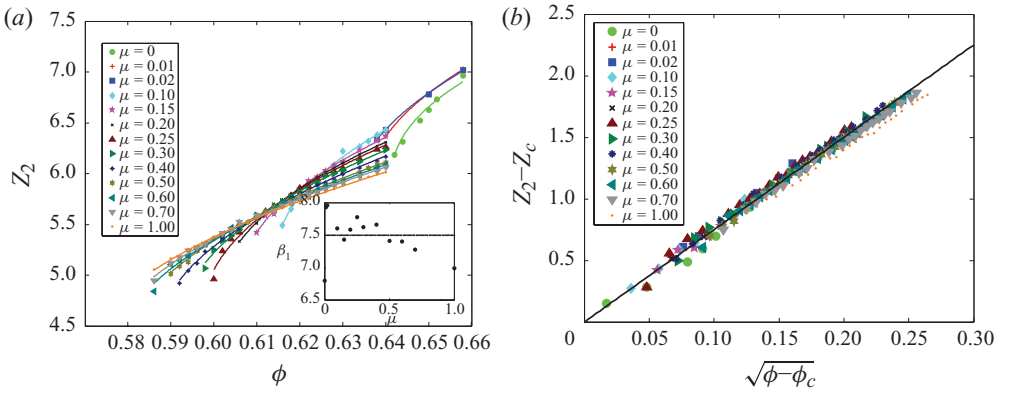

FIGURE 9. (Colour online) Coordination number variations are plotted as (*a*) Z_2 versus ϕ and (*b*) $Z_2 - Z_c$ versus $(\phi - \phi_c)^{1/2}$ from the steady simple shear DEM data (symbols) and fits (solid lines). The equations used for the fits are $Z_2 - Z_c = \beta_1(\phi - \phi_c)^{1/2}$ and $Z_2 - Z_c = 7.5(\phi - \phi_c)^{1/2}$ in (*a*) and (*b*), respectively. The inset in (*a*) shows the variation of β_1 against μ with a line indicating its mean.

vanish at steady simple shear and the relation between ϕ and Z_2 at steady shear in the third term drives coordination number to a steady value. The function $f(\phi)$ dictates how the coordination number varies with volume fraction during the steady shear. We found the scaling between Z_2 and ϕ for frictional spheres under simple shear to be essentially the same as the critical scaling near jamming transition for frictionless (O'Hern *et al.* 2003) and frictional (Zhang & Makse 2005) particles, i.e. $Z_2 - Z_c \sim (\phi - \phi_c)^{1/2}$. This is confirmed by the good fits to the DEM simple shear data using $Z_2 - Z_c = \beta_1(\phi - \phi_c)^{1/2}$ for all the μ values studied as shown in figure 9(*a*), where symbols denote DEM data and solid lines are used for the fits. The inset of figure 9(*a*) shows that the fitting parameter β_1 fluctuates in a small range about its mean value of 7.5. Plotting $Z_2 - Z_c$ against $(\phi - \phi_c)^{1/2}$, all DEM data collapse onto a band centred around the line of $Z_2 - Z_c = 7.5(\phi - \phi_c)^{1/2}$ shown in figure 9(*b*), which supports the use of a constant β_1 to represent the variations for all μ values. Therefore, the equation for $f(\phi)$ in our model takes the following form:

$$f(\phi) = Z_c + \beta_1(\phi - \phi_c)^{\beta_2}, \tag{4.9}$$

where model constants $\beta_1 = 7.5$ and $\beta_2 = 0.5$. Figure 5(*c*) displays ϕ_c determined through the curve fit above, and its correlation is listed in table 1. Constant numerical values were found to be adequate for d_1–d_3 (to capture the evolution of Z_2 through (4.8) reasonably well) and are listed in table 2. The tr($\boldsymbol{D}$) term is used to take account of the effects of compaction and dilatation on increasing and decreasing the coordination number. Thus, the Reynolds dilatancy constraint is implicitly incorporated in (4.8), which can be rewritten in an explicit form proposed by Goddard (2010), $\mathrm{tr}(\boldsymbol{D}) = \alpha|\boldsymbol{S}|$, where the coefficient of dilatancy $\alpha = (1/d_3)[(\dot{Z}_2/|\boldsymbol{S}|) - d_1(\boldsymbol{A} : \hat{\boldsymbol{S}} - \chi) - d_2(f(\phi) - Z_2)|\boldsymbol{D}/\boldsymbol{S}|]$, is dynamically changing according to the evolution of Z_2 and $\boldsymbol{A}$. The computational results from (4.8) are compared to the DEM data in figures 1(*c*) and 2(*c*). For both conditions, the Z_2 magnitudes and its evolution strain scales after shear reversal were correctly produced. The small quantitative discrepancies evident in these comparisons do not affect the pressure calculation significantly, as will be shown next.

5. Model verification

Equations (4.1), (4.2), (4.5), (4.7) and (4.8) compose a constitutive model which neglects normal stress difference. Admittedly, the model involves a number of adjustable parameters; nevertheless, it is emphasized that the number of parameters is not that many, considering that the model tracks the evolution of stress, fabric, coordination number and volume fraction under both steady and unsteady conditions for a range of particle friction coefficients. The present study is aimed at demonstrating that the microscopic physics of jamming and anisotropy can indeed be incorporated into a continuum constitutive model, at least at a semi-empirical level. A desirable resulting attribute is that all the model parameters are linked to particle scale properties.

5.1. *Model self-consistency*

The evolution of the pressure and stress ratio predicted by the model for shear flows under the CV condition is shown in figures 1(*a*) and 1(*b*) and compared with the DEM data. Although there are small quantitative differences between the model and the DEM results, the model reproduces all the key features correctly. To simulate simple shear under the CP condition, we allow tr($\boldsymbol{D}$) (in the Z_2 evolution equation) to vary while insisting that p remains invariant. The modelled evolution of the volume fraction and stress ratio, as shown in figures 2(*a*) and 2(*b*), matched the DEM data well. These comparisons reveal that the constitutive model is self-consistent and is able to correctly describe the pressure and stress ratio evolution during steady and unsteady flows of rate-independent granular materials. Similar model verification was done at several μ values (details not shown).

5.2. *Model predictions*

We now demonstrate the model's predictive capability by applying it to new unsteady shear flow situations without re-calibrating any material constants and comparing the predicted response with DEM data.

We subjected the assembly to a cyclic simple shear with small strain amplitude in the first test. The shear rate was a square-wave function with a magnitude of $\dot{\gamma}_0$ and the maximum strain in each flow direction followed γ_A. Experimental studies on cyclic shear of dense granular materials (Youd 1971; Wood & Budhu 1980; Toiya *et al.* 2004) have found that the assemblies compacted when γ_A was small and a large portion of the volume reduction occurred immediately after the shear reversal. The DEM simulation illustrated in figure 10 was performed with $\gamma_A = 0.5$ and started from a steady state where $\phi = 0.6$. The volume fraction evolution is plotted using (blue) squares in figure 10(*a*) against the accumulated strain $\dot{\gamma}_0 t$. The ϕ increased from 0.6 to about 0.61 after the first shear reversal at $\dot{\gamma}_0 t = 0.5$ and then slowly increased to about 0.62 at $\dot{\gamma}_0 t = 4$. Our model, without adjusting any of the model constants, predicts a similar compaction behaviour as shown by the (red) solid line in figure 10(*a*), but the final volume fraction is slightly higher than that of the DEM data. Figure 10(*b*) shows that the model can also predict the shear stress ratio well. The microstructural variables Z_2 and A_{xz} are shown in figures 10(*c*) and 10(*d*), respectively. The predicted Z_2 values have slightly larger discrepancies than the A_{xz} values.

For the second test, we studied the Reynolds dilatancy, i.e. the tendency of a dense granular assembly to expand in volume upon initial shearing, which was first revealed by Reynolds (1885). The Reynolds dilatancy is an essential constraint for dense granular flow and has important influence on granular plasticity. As shown in figure 11, we sheared an initially isotropic assembly at $\dot{\gamma}_0$ to a steady state under a

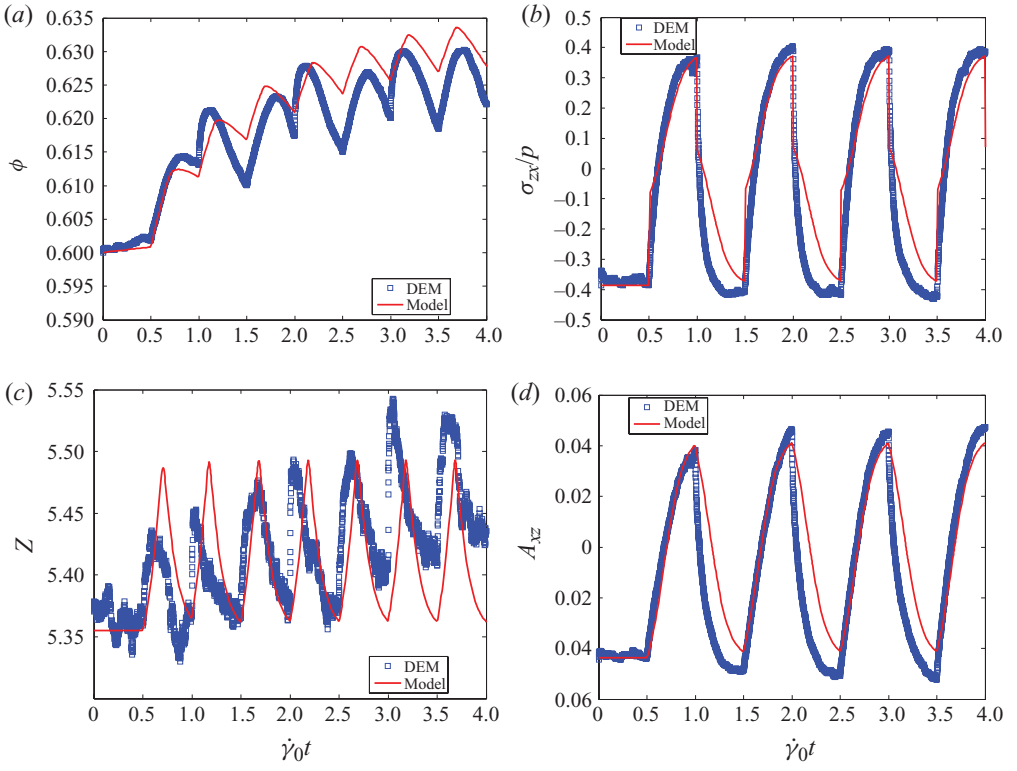

FIGURE 10. (Colour online) Evolution of (*a*) volume fraction, (*b*) stress ratio, (*c*) coordination number and (*d*) A_{xz} for an assembly subjected to small-amplitude oscillatory shear under the constant pressure condition with $pd/k \approx 0.01$. Blue square symbols denote the data from DEM simulations and the red solid curves are the constitutive model results. The interparticle friction coefficient μ is 0.5 and the inertia number $I \approx 0.0003$ at steady state.

constant pressure. The DEM data indicate the dilatancy, i.e. ϕ decreased from about 0.612 to 0.602 (see figure 11*a*). We note that there was an initial densification before the dilatation, which was also observed in experiments with sand (Okada & Nemat-Nasser 1994). The shear stress ratio quickly reached the steady state in figure 11(*b*), as did Z_2 and A_{xz} (see figure 11*c, d*). Our model results denoted by the (red) solid lines in figure 11 predicted the correct dilatancy behaviour and also the correct trends for stress ratio and microstructural variables. The model also provides a microscopic explanation for the Reynolds dilatancy. Since the shear flow increases the anisotropy magnitude of the assembly, the coordination number has to decrease as dictated by the pressure equation (4.2) to keep a constant pressure. The coordination number evolution equation in turn requires a dilatation to achieve this decrease in Z_2. Therefore, shearing an initially isotropic assembly of frictional particles leads to the Reynolds dilatancy. In contrast, shearing frictionless (spherical) particles does not lead to measurable dilatancy, as the anisotropy does not affect the pressure for frictionless particles (according to (4.2)).

6. Summary

We have proposed a constitutive model for the rate-independent rheology of dense granular materials subjected to simple shear. It is suitable for flows where $|\mathrm{tr}(\hat{\boldsymbol{D}})| \ll 1$

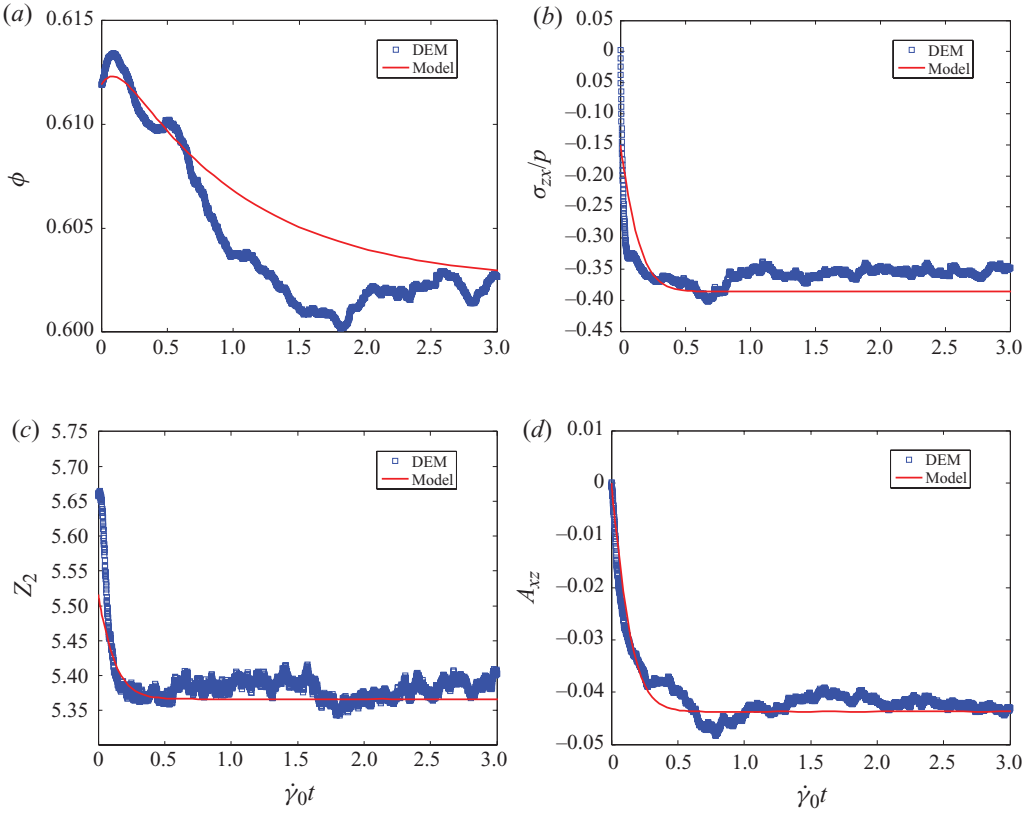

FIGURE 11. (Colour online) Evolution of (*a*) volume fraction, (*b*) stress ratio, (*c*) coordination number and (*d*) A_{xz} for an assembly subjected to shear start from an isotropic condition under the constant pressure condition with $pd/k \approx 0.01$. Blue square symbols denote the data from DEM simulations and the red solid curves are the constitutive model results. The interparticle friction coefficient μ is 0.5 and the inertia number $I \approx 0.0003$ at steady state.

(but need not to be zero), which includes a wide range of practical flow problems. The model for stress (4.1) consists of a pressure term and a deviatoric term with a macroscopic friction coefficient. The closures for the pressure and the friction coefficient ((4.2) and (4.5)) are linked to two microstructural variables, namely the fabric and the average coordination number (excluding floaters and rattlers), whose evolution is modelled by (4.7) and (4.8). For the Hookean model, the pressure is given by (4.2). The analogous form for a Hertzian model can be deduced from (4.4) as $p_{Hz}/k_{Hz} \approx (a_1 + a_2|\boldsymbol{A}|)^{3/2}(Z_2 - Z_c)^3$. The material constants in the model are functions of particle-level properties and were calibrated using shear flow DEM data. We have verified the model's self-consistency by reproducing the steady and unsteady DEM data used in the calibration. We have also demonstrated its predictive capability through cyclic shear and Reynolds dilatancy tests.

The authors are grateful to professors Joe Goddard, Prabhu Nott, Kesava Rao and Stefan Luding for their stimulating discussions on continuum modelling of dense granular materials. We appreciate the constructive and helpful comments from the reviewers. We also thank Sebastian Chialvo for generating part of the DEM data. This work was supported by a DOE-UCR grant DE-FG26-07NT43070.

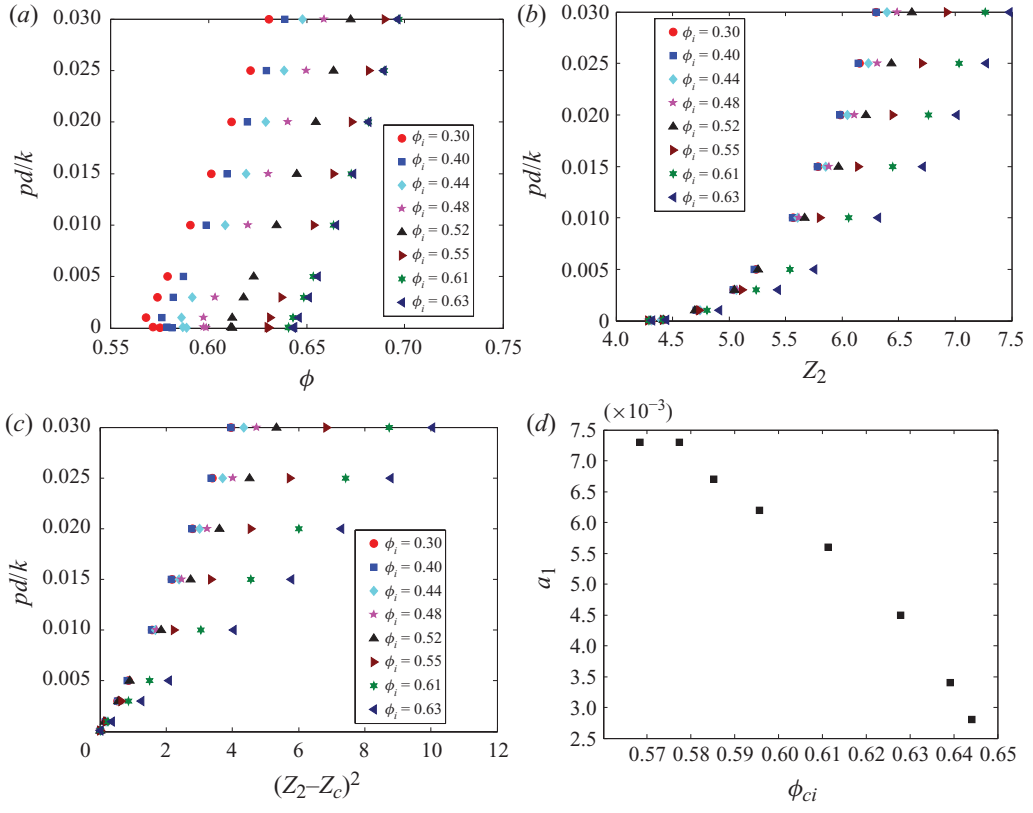

FIGURE 12. (Colour online) Scaled pressure varies with (*a*) volume fraction ϕ and (*b*) coordination number Z_2 during isotropic compression simulations starting from different initial volume fractions ϕ_i. The same data in (*b*) are re-plotted against $(Z_2 - Z_c)^2$ in (*c*). The variation of the pre-factor a_1^* in the (pd/k)–$(Z_2 - Z_c)^2$ relation is plotted against jamming volume fractions in (*d*). The error bars for the standard deviations of ϕ and Z_2 values resulted from the three realizations performed are comparable to the symbol size and thus not plotted in the figures. Particles in the assemblies have interparticle friction coefficient $\mu = 0.5$.

Appendix A. Normal stress differences

We first identify the characteristics of a stress tensor during steady simple shear by plotting the stress components scaled by pressure against volume fraction in figure 13. It can be seen that scaled stress magnitudes are not very sensitive to the volume fraction variation. Normal stress components are different from each other with a deviation of 5 %–10 % from the mean pressure (see figure 13*a*). It is also seen that the magnitude of the first normal stress difference (Barnes, Hutton & Walters 1989), $N_1 = \sigma_{xx} - \sigma_{zz}$, is about one third to that of the second normal stress difference, $N_2 = \sigma_{zz} - \sigma_{yy}$. Only the σ_{zx} $(= \sigma_{xz})$ shear stress component is non-trivial while others are very close to zero (see figure 13*b*). The parity plot of the shear stress components in the inset to figure 13(*b*) shows that the stress tensor is approximately symmetric for these homogeneous shear flows, although it could be asymmetric near walls or in shear bands (Mohan, Rao & Nott 2002).

According to (4.1) in the basic model, the normal stress components are equal under simple shear, i.e. $\sigma_{xx} = \sigma_{yy} = \sigma_{zz} = p$. This is not consistent with the normal stress difference observed from our DEM simulation results (e.g. see figure 13) and

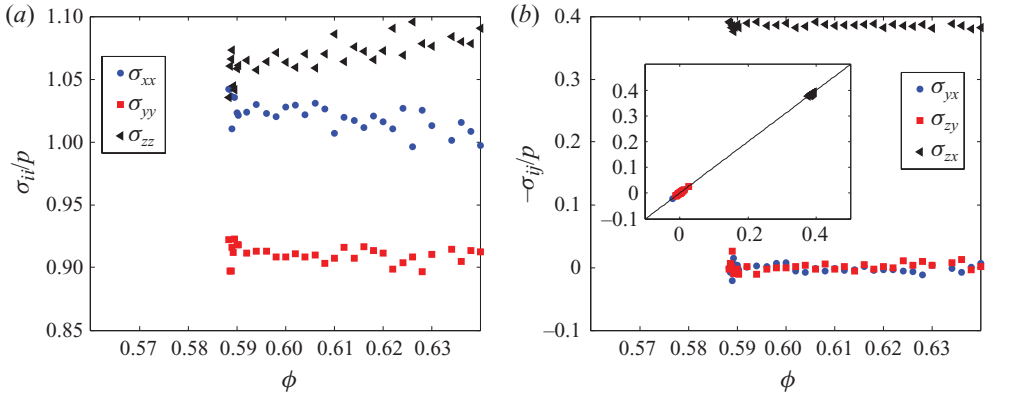

FIGURE 13. (Colour online) (*a*) Normal and (*b*) shear stress components scaled by the pressure are plotted against volume fraction ϕ during steady simple shear under both constant volume and constant pressure conditions. The inset in (*b*) is the parity plot of the symmetric parts of the shear stress components, such as σ_{xz} versus σ_{zx}. The interparticle friction coefficient μ is 0.5 and the inertia number $I < 0.001$.

experimental data (for example, reported by Savage 1979 for neutrally buoyant suspensions). We now extend the basic model in two stages to capture the normal stress differences: first, to capture the normal stress component with the largest deviation from the mean pressure, i.e. σ_{yy} and represent σ_{xx} and σ_{zz} by their mean value, $\bar{\sigma}_{13} = \frac{1}{2}(\sigma_{xx} + \sigma_{zz})$; second, to further capture the difference between σ_{xx} and σ_{zz}. In terms of the first and second normal stress differences, N_1 and N_2, we first model $\frac{1}{2}N_1 + N_2$ (since $\bar{\sigma}_{13} - \sigma_{yy} = \frac{1}{2}N_1 + N_2$) and then model N_1.

We first model $\bar{\sigma}_{13}$ and σ_{yy} components by augmenting the stress equation as

$$\boldsymbol{\sigma} = p\boldsymbol{I} - p\eta\hat{\boldsymbol{S}} + a_3 p\left(\boldsymbol{A}\hat{\boldsymbol{S}} + \hat{\boldsymbol{S}}\boldsymbol{A} - \tfrac{2}{3}(\boldsymbol{A} : \hat{\boldsymbol{S}})I\right). \tag{A 1}$$

The augmented equation (A 1) has the property that the pressure and the deviatoric stress components derived from it are not altered from those in the basic equation (4.1) as this additional term is traceless and the deviatoric parts in $\boldsymbol{A}\hat{\boldsymbol{S}}$ and $\hat{\boldsymbol{S}}\boldsymbol{A}$ cancel each other for simple shear flows. Therefore, the material parameters determined in the basic model need not be recalibrated for this augmented stress equation. For steady simple shear flows, the normal stress components take the following forms:

$$\left.\begin{aligned} \sigma_{xx} = \sigma_{zz} = \bar{\sigma}_{13} &= p\left(1 + \tfrac{2}{3}a_3 A_{xz}\mathrm{sgn}(\dot{\gamma})\right), \\ \sigma_{yy} &= p\left(1 - \tfrac{4}{3}a_3 A_{xz}\mathrm{sgn}(\dot{\gamma})\right), \end{aligned}\right\} \tag{A 2}$$

where $\mathrm{sgn}(\dot{\gamma})$ is the sign of shear rate. Therefore,

$$\tfrac{1}{2}N_1 + N_2 = 2a_3 p A_{xz}\mathrm{sgn}(\dot{\gamma}). \tag{A 3}$$

According to (A 2), the difference between σ_{yy} and the mean pressure p is exactly twice of that between $\bar{\sigma}_{13}$ and p, which will be shown to be supported by our DEM data.

To calibrate the parameter a_3, we used the steady shear DEM data. Figure 14(*a*) compares the predictions of the augmented model of $\bar{\sigma}_{13}$ and σ_{yy} scaled by pressure with the steady shear DEM data for assemblies of particles with $\mu = 0.5$ and $\mu = 0.1$. When applied to unsteady shear, the augmented model agrees with most of the variation although the instantaneous values at shear reversal are overpredicted, as shown in figure 14(*b*) for a reversal under the constant volume condition. The

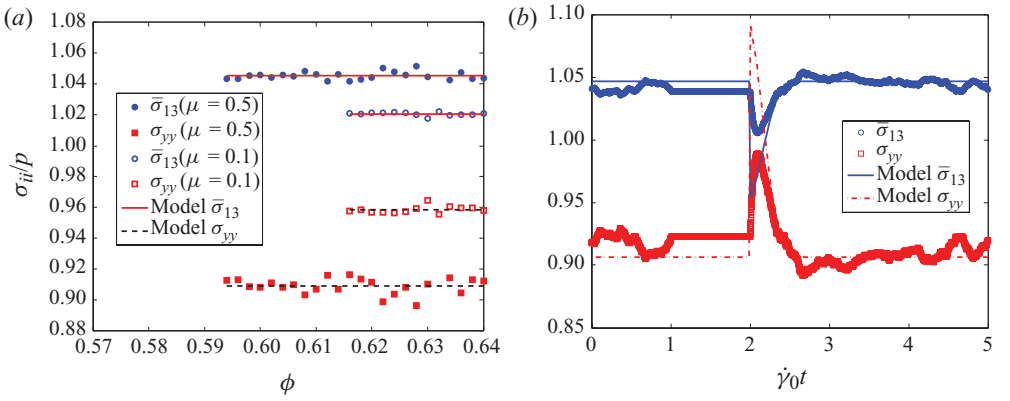

FIGURE 14. (Colour online) Normal stress components $\bar{\sigma}_{13}$ and σ_{yy} scaled by pressure are plotted against volume fraction and shear strain for an assembly in (*a*) steady simple shear and (*b*) unsteady shear under the constant volume condition, respectively. Symbols denote data from DEM simulations and curves are the constitutive model results. In (*a*), solid symbols denote particles with $\mu = 0.5$ and open symbols denote $\mu = 0.1$. In (*b*), particle friction coefficient is 0.5 and volume fraction is 0.6.

overprediction is caused by the constant a_3 used in the model. The prediction of unsteady behaviour can be improved by making a_3 vary with microstructure evolution, which was not pursued in this paper.

The second stage of the extension aimed at modelling the first normal stress difference N_1 leads to

$$\boldsymbol{\sigma} = p\boldsymbol{I} - p\eta\hat{\boldsymbol{S}} + a_3 p\left(\boldsymbol{A}\hat{\boldsymbol{S}} + \hat{\boldsymbol{S}}\boldsymbol{A} - \tfrac{2}{3}(\boldsymbol{A} : \hat{\boldsymbol{S}})I\right) + a_4 p\left(\boldsymbol{A} - \tfrac{1}{2}(\boldsymbol{A} : \hat{\boldsymbol{S}})\hat{\boldsymbol{S}}\right). \tag{A 4}$$

The normal stress components take the following forms for simple shear flows:

$$\left.\begin{aligned} \sigma_{xx} &= p\left(1 + \tfrac{2}{3}a_3 A_{xz}\mathrm{sgn}(\dot{\gamma}) + a_4 A_{xx}\right), \\ \sigma_{zz} &= p\left(1 + \tfrac{2}{3}a_3 A_{xz}\mathrm{sgn}(\dot{\gamma}) + a_4 A_{zz}\right), \\ \sigma_{yy} &= p\left(1 - \tfrac{4}{3}a_3 A_{xz}\mathrm{sgn}(\dot{\gamma})\right). \end{aligned}\right\} \tag{A 5}$$

As prescribed in the fabric evolution equation (4.7), $A_{xx} = -A_{zz}$ and $A_{yy} = 0$, which is supported by our DEM data (Aarons *et al.* 2009). The first and second normal stress differences are thus fully resolved as

$$\left.\begin{aligned} N_1 &= \quad \sigma_{xx} - \sigma_{zz} = a_4 p(A_{xx} - A_{zz}), \\ N_2 &= \sigma_{zz} - \sigma_{yy} = a_3 p A_{xz}\mathrm{sgn}(\dot{\gamma}) + a_4 p A_{zz}, \end{aligned}\right\} \tag{A 6}$$

which implies that the first normal stress difference is caused by the difference between the corresponding fabric normal components. As both A_{xx} and A_{zz} are small in magnitude, the magnitude of N_1 is also small, which is supported by our DEM data shown below.

We used the DEM normal stress and fabric data of steady simple shear averaged over a range of volume fractions to calibrate a_4. We then compared the predictions of the normal stress components scaled by pressure to the corresponding DEM data for assemblies of particles with friction coefficients $\mu = 0.5$ and $\mu = 0.1$ in figures 15(*a*) and 15(*b*), respectively. It can be seen that both the first and second normal stress differences are captured and agree well with the DEM data for both different μ values. When applied to a shear reversal flow under constant volume condition, the further augmented model captured most of the trends, but some quantitative differences

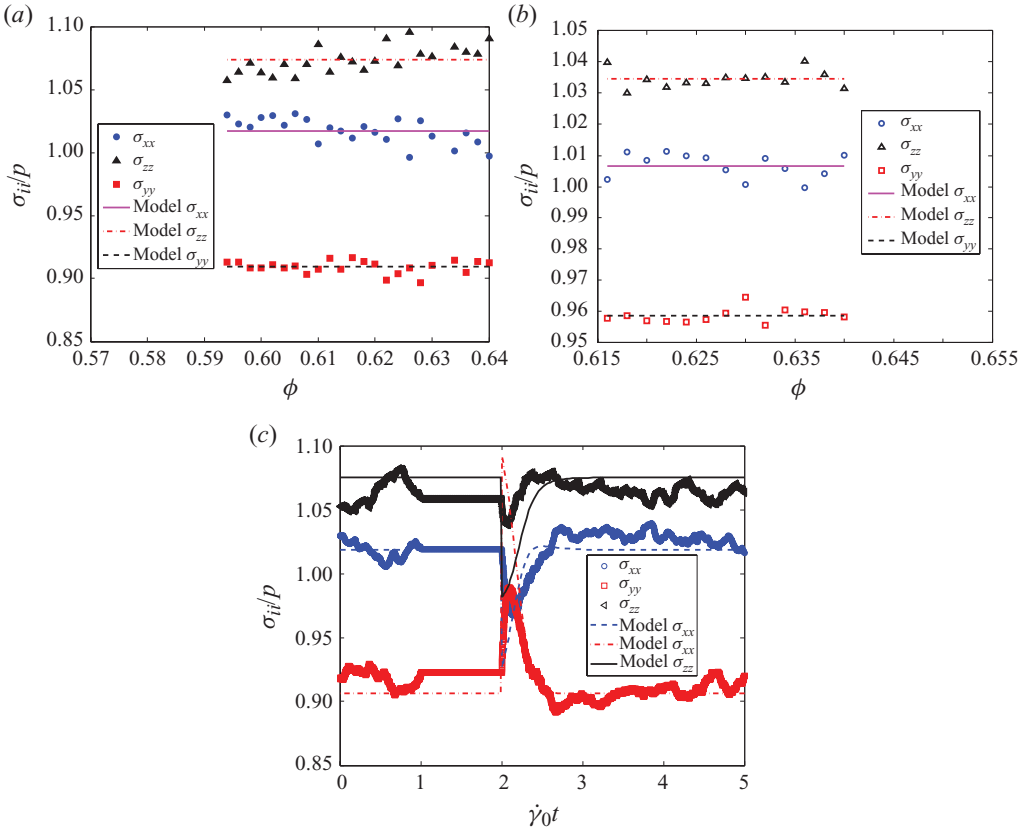

FIGURE 15. (Colour online) Normal stress components σ_{xx}, σ_{yy} and σ_{zz} scaled by pressure are plotted against volume fraction and shear strain for an assembly in (*a*) steady simple shear with particle friction coefficient $\mu = 0.5$, (*b*) steady simple shear with particle friction coefficient $\mu = 0.1$ and (*c*) unsteady shear under the constant volume condition, respectively. Symbols denote data from DEM simulations and curves denote the constitutive model results. In (*c*), particle friction coefficient is 0.5 and volume fraction is 0.6.

remain as shown in figure 15(*c*). The main difference is again the overprediction at shear reversal caused by the constant a_4.

The normal stress difference increases monotonically with increasing particle friction coefficient μ. This trend is reflected by parameters a_3 and a_4 increasing in magnitude as reported in figures 16(*a*) and 16(*b*), which can be fitted using the equations $a_3 = 1.57\mathrm{e}^{-4.5\mu} - 1.7$ and $a_4 = -6.5\mathrm{e}^{-2\mu} + 6.5$, respectively.

The full model, consisting of (A 4) for stress, (4.2) for pressure, (4.5) for macroscopic friction coefficient, (4.7) for fabric evolution and (4.8) for coordination number evolution, can be simplified for steady simple shear flows as follows. For these flows, the strain rate tensor $\hat{\boldsymbol{D}}$ takes the form $\mathrm{sgn}(\dot{\gamma})(\boldsymbol{e}_{(x)}\boldsymbol{e}_{(z)} + \boldsymbol{e}_{(z)}\boldsymbol{e}_{(x)})$ and $\hat{\boldsymbol{S}} = \hat{\boldsymbol{D}}$. The expressions for steady state $\boldsymbol{A} : \hat{\boldsymbol{S}}$, $|\boldsymbol{A}|$ and $\boldsymbol{A} \cdot \hat{\boldsymbol{S}}$, deduced by taking the corresponding double-dot and dot products with the equation for steady state of the fabric evolution (4.7), are

$$\boldsymbol{A} : \hat{\boldsymbol{S}} = -\frac{c_2 + \sqrt{c_2^2 - 8c_1c_3}}{2c_3} := \chi, \tag{A 7}$$

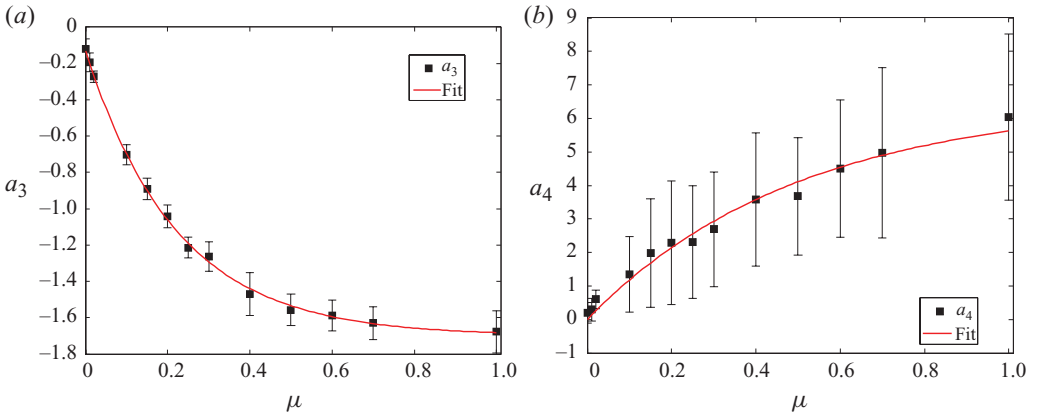

FIGURE 16. (Colour online) Variation of parameters (*a*) a_3 and (*b*) a_4 versus friction coefficient μ. The equations used for the fitting curve in (*a*) and (*b*) are $a_3 = 1.57\mathrm{e}^{-4.5\mu} - 1.7$ and $a_4 = -3.7\mathrm{e}^{-1.2\mu} + 4$, respectively.

$$|\boldsymbol{A}| = \sqrt{\frac{-c_1\chi}{2(c_2 + c_3\chi)}} := \kappa, \tag{A 8}$$

and

$$\boldsymbol{A}\cdot\hat{\boldsymbol{S}} = -\frac{c_1}{c2 + c_3\chi}\hat{\boldsymbol{S}}\cdot\hat{\boldsymbol{S}} := \lambda\hat{\boldsymbol{S}}\cdot\hat{\boldsymbol{S}}, \tag{A 9}$$

respectively. In the deduction of (A 7) and (A 9), the rotational contribution in the Jaumann derivative, i.e. $\boldsymbol{A}\cdot\boldsymbol{W} - \boldsymbol{W}\cdot\boldsymbol{A}$, was neglected, which implies zero normal fabric components according to (4.7) and thus zero first normal stress difference. For applications where the first normal stress difference is not of serious concern, one can employ the following simplified version of the model. Substituting (A 9) to the stress (A 4), (4.9) and (A 8) to the pressure (4.2) and (A 7) to the macroscopic friction coefficient (4.5), we obtain the simplified stress, pressure and friction coefficient and equations,

$$\boldsymbol{\sigma} = p\boldsymbol{I} - p\eta\hat{\boldsymbol{S}} + 2a_3 p\left(\lambda\hat{\boldsymbol{S}}\cdot\hat{\boldsymbol{S}} - \tfrac{1}{3}\chi\boldsymbol{I}\right), \tag{A 10}$$

$$pd/k = (a_1 + a_2\kappa)\beta_1^2(\phi - \phi_c) \tag{A 11}$$

and

$$\eta = b_1 + b_2\chi, \tag{A 12}$$

respectively. The microstructural variables do not appear directly in this model as there is no need to evolve them. One can further truncate this model, if adequate for specific applications, by only retaining the first two terms on the right-hand side of (A 10). This highly simplified model has a very familiar form (Savage 1983; Jackson 1986), but all the parameters are now linked to particle-scale properties.

Appendix B. Isotropic compression pressure data and model

We used the following protocol to prepare isotropic assemblies under different levels of confining pressure. Particles were first treated as elastic, frictionless spheres and thermalized and equilibrated over a broad range of volume fractions up to $\phi_i = 0.63$ in a cubic periodic domain. The particles were then assigned the desired friction coefficient and inelasticity, and compressed isotropically at a very slow rate

to a finite pressure level, at which mechanical equilibrium was maintained for a long period of time (usually $>10^7$ DEM time steps). At this stage, jamming point, where static pressure is zero, was crossed. Thus, the jamming point can be approached by performing simulations for lower and lower final pressure. This protocol is analogous to that used by Song *et al.* (2008), where the volume fraction after compression was controlled instead of pressure. Many realizations with different disordered initial configurations were performed for each ϕ_i value and each pressure level to achieve good statistics.

Volume fractions and coordination numbers during the equilibrium states at pressure levels ranging from $pd/k = 10^{-5}$ to $pd/k = 3 \times 10^{-2}$ are reported in figures 12(*a*) and 12(*b*), respectively, for particle assembly with $\mu = 0.5$. The jamming points, ϕ_{ci} and Z_c, can be determined by extrapolating the results to the zero-pressure limit using data in these two figures. It can be seen that pressure has a nearly linear scaling with $(\phi - \phi_{ci})$ and a quadratic scaling with $(Z_2 - Z_c)$, which is consistent with previous findings (using the Hookean contact model) of O'Hern *et al.* (2003). The quadratic scaling is also indicated by the linearity between pd/k and $(Z_2 - Z_c)^2$ in figure 12(*c*). A comparison of the results of simulations starting from eight ϕ_i values ($\phi_i =$ 0.3, 0.4, 0.44, 0.48, 0.52, 0.55, 0.61 and 0.63) reveals that the critical volume fraction for jamming, ϕ_{ci}, is not unique; however, the critical coordination number for jamming, Z_c, is, which has also been reported in other studies (Song *et al.* 2008; Chaudhuri, Berthier & Sastry 2010). The uniqueness of Z_c is one of the reasons for modelling the pressure as a function of Z_2 instead of ϕ. Although the pd/k versus Z_2 curves with different ϕ_i values appear to collapse onto a master curve at the vicinity of Z_c as reported by Chaudhuri *et al.* (2010), they diverge at higher pressure or larger Z_2 values. Simulations for different μ values were repeated with similar findings.

To take account of this history dependence on packing preparation, an additional variable, compactivity X, needs to be introduced into the model. It may be interpreted as a measure of the number of different ways of arranging the grains in the system into a volume with certain degree of disorder. The two limits, $X = 0$ and $+\infty$, correspond to the most and least compact stable arrangements. Compactivity can be shown to be a function of Z and ϕ and can be calculated using the statistical theory developed by Song *et al.* (2008) and Briscoe *et al.* (2010). Using the compactivity and the scaling observed in figure 12(*c*), the isotropic pressure can be modelled as

$$pd/k = (a_1|_{(X_c \to +\infty)} + g(X_c)\mathrm{tr}(\hat{\boldsymbol{D}})) * (Z_2 - Z_c)^2 := a_1^*(Z_2 - Z_c)^2, \tag{B 1}$$

where $g(X_c)$ is a function of X_c, the compactivity at jamming point and $\mathrm{tr}(\hat{\boldsymbol{D}}) = -\sqrt{6}$ for isotropic compression. The $\mathrm{tr}(\hat{\boldsymbol{D}})$ term is zero in simple shear under the constant volume condition and its order of magnitude is much less than one for most dynamical systems involving significant deviatoric deformations. This term reflects the fact that the dependence on packing preparation vanishes after shearing for a substantial strain as shown in the text. To illustrate the functional dependence of a_1^* on X_c without an elaborate effort of calculating X_c, we plot a_1^* against ϕ_{ci} in figure 12(*d*) as X_c only depends on ϕ_{ci} at a fixed Z_c. It can be seen that there is a smooth functional dependence and $a_1^* \to a_1$ as $X_c \to +\infty$ at the lowest two ϕ_{ci} values (corresponding to $\phi_i = 0.4$ and $\phi_i = 0.3$).

Although the isotropic pressure can be represented formally using (B 1), for the purpose of modelling of large-strain-scale flow behaviour, we simplify the equation by retaining only the a_1 term, which is the leading and asymptotic term. This simplification is applicable to assemblies constructed with $|\mathrm{tr}(\hat{\boldsymbol{D}})| \ll 1$ and is also

consistent with the configurations of most granular assemblies in engineering practice that are usually constructed from low volume fractions. This simplified equation is used in the pressure equation (4.2) in the text.

REFERENCES

Aarons, L. R., Sun, J. & Sundaresan, S. 2009 Unsteady shear of dense assemblies of cohesive granular materials under constant volume conditions. *Ind. Engng Chem. Res.* **49** (11), 5153–5165.

Anand, L. & Gu, C. 2000 Granular materials: constitutive equations and strain localization. *J. Mech. Phys. Solids* **48** (8), 1701–1733.

Azéma, E., Radjai, F. & Saussine, G. 2009 Quasistatic rheology, force transmission and fabric properties of a packing of irregular polyhedral particles. *Mech. Mater.* **41** (6), 729–741.

Barnes, H. A., Hutton, J. F. & Walters, K. 1989 *An Introduction to Rheology*. Elsevier.

Bathurst, R. J. & Rothenburg, L. 1990 Observations on stress-force-fabric relationships in idealized granular materials. *Mech. Mater.* **9** (1), 65–80.

Bocquet, L., Losert, W., Schalk, D., Lubensky, T. C. & Gollub, J. P. 2001 Granular shear flow dynamics and forces: Experiment and continuum theory. *Phys. Rev.* E **65** (1), 011307.

Briscoe, C., Song, C., Wang, P. & Makse, H. A. 2010 Jamming III: Characterizing randomness via the entropy of jammed matter. *Physica* A **389** (19), 3978–3999.

Campbell, C. S. 2002 Granular shear flows at the elastic limit. *J. Fluid Mech.* **465**, 261–291.

Chaudhuri, P., Berthier, L. & Sastry, S. 2010 Jamming transitions in amorphous packings of frictionless spheres occur over a continuous range of volume fractions. *Phys. Rev. Lett.* **104** (16), 165701.

da Cruz, F., Emam, S., Prochnow, M., Roux, J-N. & Chevoir, F. 2005 Rheophysics of dense granular materials: Discrete simulation of plane shear flows. *Phys. Rev.* E **72** (2), 021309.

Cundall, P. A. & Strack, D. L. 1979 A discrete numerical model for granular assemblies. *Géotechnique* **29**, 47–65.

Drucker, D. C., Gibson, R. E. & Henkel, D. J. 1957 Soil mechanics and work hardening theories of plasticity. *Trans. Am. Soc. Civil Engng* **122**, 338–346.

Evans, D. J. & Morriss, G. P. 1990 *Statistical Mechanics of Nonequilibrium Liquids*. *Theoretical chemistry* 1. Academic Press.

Gadala-Maria, F. & Acrivos, A. 1980 Shear-induced structure in a concentrated suspension of solid spheres. *J. Rheol.* **24** (6), 799–814.

Gera, D., Syamlal, M. & O'Brien, T. J. 2004 Transport equation for modeling particle contacts. In *11th Intl Conf. on Fluidization* (ed. U. Arena, R. Chirone, M. Miccio & P. Salatino). Engineering Conferences International.

Goddard, J. 1986 Dissipative materials as constitutive models for granular media. *Acta Mechanica* **63** (1), 3–13.

Goddard, J. 2010 Parametric hypoplasticity as continuum model for granular media: from Stokesium to Mohr–Coulombium and beyond. *Granular Matter* **12** (2), 145–150.

Goddard, J. D. 1984 Dissipative materials as models of thixotropy and plasticity. *J. Non-Newtonian Fluid Mech.* **14**, 141–160.

Goddard, J. D. 1998 Continuum modeling of granular assemblies. In *Physics of Dry Granular Media* (ed. H. J. Herrmann), chap. 1, pp. 1–24. Kluwer.

Goddard, J. D. 2006 A dissipative anisotropic fluid model for non-colloidal particle dispersions. *J. Fluid Mech.* **568** (1), 1–17.

Harris, D. 2006 Some properties of a new model for slow flow of granular materials. *Meccanica* **41** (3), 351–362.

Hébraud, P. & Lequeux, F. 1998 Mode-coupling theory for the pasty rheology of soft glassy materials. *Phys. Rev. Lett.* **81** (14), 2934–2937.

Hill, R. 1950 *The Mathematical Theory of Plasticity*. Oxford University Press.

Jackson, R. 1986 Some features of the flow of granular materials and aerated granular materials. *J. Rheol.* **30** (5), 907–930.

Ketterhagen, W. R., Curtis, J. S., Wassgren, C. R. & Hancock, B. C. 2009 Predicting the flow mode from hoppers using the discrete element method. *Powder Technol.* **195** (1), 1–10.

Keys, A. S., Abate, A. R., Glotzer, S. C. & Durian, D. J. 2007 Measurement of growing dynamical length scales and prediction of the jamming transition in a granular material. *Nat. Phys.* **3** (4), 260–264.

Kheiripour Langroudi, M., Sun, J., Sundaresan, S. & Tardos, G. I. 2010 Transmission of stresses in static and sheared granular beds: The influence of particle size, shearing rate, layer thickness and sensor size. *Powder Technol.* **203** (1), 23–32.

Lade, P. V. 1977 Elasto-plastic stress-strain theory for cohesionless soil with curved yield surfaces. *Intl J. Solids Struct.* **13** (11), 1019–1035.

Lees, A. W. & Edwards, S. F. 1972 The computer study of transport processes under extreme conditions. *J. Phys.* C **5** (15), 1921–1928.

Lu, K., Brodsky, E. E. & Kavehpour, H. P. 2007 Shear-weakening of the transitional regime for granular flow. *J. Fluid Mech.* **587** (1), 347–372.

Luding, S. 2004 Micro–macro transition for anisotropic, frictional granular packings. *Intl J. Solids Struct.* **41** (21), 5821–5836.

Luding, S. 2005 Anisotropy in cohesive, frictional granular media. *J. Phys. Condens. Matter* **17** (24), 2623–2640.

Majmudar, T. S. & Behringer, R. P. 2005 Contact force measurements and stress-induced anisotropy in granular materials. *Nature* **435** (7045), 1079–1082.

Majmudar, T. S., Sperl, M., Luding, S. & Behringer, R. P. 2007 Jamming transition in granular systems. *Phys. Rev. Lett.* **98** (5), 058001.

Makse, H., Johnson, D. L. & Schwartz, L. M. 2000 Packing of compressible granular materials. *Phys. Rev. Lett.* **84** (18), 4160–4163.

Mehrabadi, M. M. & Cowin, S. C. 1978 Initial planar deformation of dilatant granular materials. *J. Mech. Phys. Solids* **26** (4), 269–284.

MiDi, G. D. R. 2004 On dense granular flows. *Eur. Phys. J.* E **14** (4), 341–305.

Mohan, L. S., Rao, K. K. & Nott, P. R. 2002 A frictional Cosserat model for the slow shearing of granular materials. *J. Fluid Mech.* **457** (1), 377–409.

Mueth, D. M., Debregeas, G. F., Karczmar, G. S., Eng, P. J., Nagel, S. R. & Jaeger, H. M. 2000 Signatures of granular microstructure in dense shear flows. *Nature* **406** (6794), 385–389.

Nedderman, R. M. 1992 *Statics and Kinematics of Granular Materials*. Cambridge University Press.

Nemat-Nasser, S. 2000 A micromechanically-based constitutive model for frictional deformation of granular materials. *J. Mech. Phys. Solids* **48** (6–7), 1541–1563.

Oda, M., Konishi, J. & Nemat-Nasser, S. 1980 Some experimentally based fundamental results on the mechanical behaviour of granular materials. *Géotechnique* **30** (4), 479–495.

O'Hern, C. S., Silbert, L. E., Liu, A. J. & Nagel, S. R. 2003 Jamming at zero temperature and zero applied stress: The epitome of disorder. *Phys. Rev.* E **68** (1), 011306.

Okada, N. & Nemat-Nasser, S. 1994 Energy dissipation in inelastic flow of saturated cohesionless granular media. *Géotechnique* **44**, 1–19.

Peyneau, P.-E. & Roux, J.-N. 2008 Frictionless bead packs have macroscopic friction, but no dilatancy. *Phys. Rev.* E **78** (1), 011307.

Plimpton, S. 1995 Fast parallel algorithms for short-range molecular dynamics. *J. Comput. Phys.* **117** (1), 1–19.

Radjai, F., Wolf, D. E., Jean, M. & Moreau, J.-J. 1998 Bimodal character of stress transmission in granular packings. *Phys. Rev. Lett.* **80** (1), 61–64.

Reynolds, O. 1885 On the dilatancy of media composed of rigid particles, with experimental illustrations. *Phil. Mag.* **20** (127), 469–481.

Rothenburg, L. & Kruyt, N. P. 2004 Critical state and evolution of coordination number in simulated granular materials. *Intl J. Solids Struct.* **41** (21), 5763–5774.

Rycroft, C. H., Kamrin, K. & Bazant, M. Z. 2009 Assessing continuum postulates in simulations of granular flow. *J. Mech. Phys. Solids* **57** (5), 828–839.

Savage, S. B. 1979 Gravity flow of cohesionless granular materials in chutes and channels. *J. Fluid Mech.* **92**, 53–96.

Savage, S. B. 1983 Granular flows down rough inclines – review and extension. In *Mechanics of Granular Materials: New Models and Constitutive Relations* (ed. J. T. Jenkins & M. Satake), pp. 261–282. Elsevier.

Savage, S. B. & Sayed, M. 1984 Stresses developed by dry cohesionless granular materials sheared in an annular shear cell. *J. Fluid Mech.* **142** (1), 391–430.

Schaeffer, D. G. 1987 Instability in the evolution equations describing incompressible granular flow. *J. Differ. Equ.* **66**, 19–50.

Schofield, A. & Wroth, P. 1968 *Critical State Soil Mechanics*. McGraw-Hill.

Shäfer, J., Dippel, S. & Wolf, D. E. 1996 Force schemes in simulations of granular materials. *J. Phys.* I **6** (1), 5–20.

Shundyak, K., van Hecke, M. & van Saarloos, W. 2007 Force mobilization and generalized isostaticity in jammed packings of frictional grains. *Phys. Rev.* E **75** (1), 010301(R).

Silbert, L. E., Ertas, D., Grest, G. S., Halsey, T. C., Levine, D. & Plimpton, S. J. 2001 Granular flow down an inclined plane: Bagnold scaling and rheology. *Phys. Rev.* E **64** (5), 051302.

Silbert, L. E., Grest, G. S., Brewster, R. & Levine, A. J. 2007 Rheology and contact lifetimes in dense granular flows. *Phys. Rev. Lett.* **99** (6), 068002.

Somfai, E., van Hecke, M., Ellenbroek, W. G., Shundyak, K. & van Saarloos, W. 2007 Critical and noncritical jamming of frictional grains. *Phys. Rev.* E **75** (2), 020301.

Song, C., Wang, P. & Makse, H. A. 2008 A phase diagram for jammed matter. *Nature* **453** (7195), 629–632.

Spencer, A. J. M. 1964 A theory of the kinematics of ideal soils under plane strain conditions. *J. Mech. Phys. Solids* **12** (5), 337–351.

Subhash, G., Nemat-Nasser, S., Mehrabadi, M. M. & Shodj, H. M. 1991 Experimental investigation of fabric–stress relations in granular materials. *Mech. Mater.* **11** (2), 87–106.

Suiker, A. S. J. & Fleck, N. A. 2004 Frictional collapse of granular assemblies. *J. Appl. Mech.* **71** (3), 350–358.

Tardos, G. I., McNamara, S. & Talu, I. 2003 Slow and intermediate flow of a frictional bulk powder in the Couette geometry. *Powder Technol.* **131** (1), 23–39.

Thornton, C. 2000 Numerical simulations of deviatoric shear deformation of granular media. *Géotechnique* **50** (1), 43–53.

Toiya, M., Stambaugh, J. & Losert, W. 2004 Transient and oscillatory granular shear flow. *Phys. Rev. Lett.* **93** (8), 088001.

Utter, B. & Behringer, R. P. 2004 Transients in sheared granular matter. *Eur. Phys. J.* E **14** (4), 373–380.

Wood, D. M. & Budhu, M. 1980 The behaviour of Leighton Buzzard sand in cyclic simple shear tests. In *Soilds under Cyclic and Transient Loading* (ed. G. N. Pande & O. C. Zienkiewicz), p. 9. Balkema.

Youd, T. L. 1971 Maximum density of sand by repeated straining in simple shear. *Highway Res. Rec.* **374**, 1–6.

Zhang, H. P. & Makse, H. A. 2005 Jamming transition in emulsions and granular materials. *Phys. Rev.* E **72** (1), 011301.

Zhu, H., Mehrabadi, M. M. & Massoudi, M. 2006 Incorporating the effects of fabric in the dilatant double shearing model for planar deformation of granular materials. *Intl J. Plast.* **22** (4), 628–653.